Overview of the Equatorial Electrojet and Related Ionospheric Current Systems

John P. Casey
Communications, Imaging, and EW Sensors Department

NAVSEA
WARFARE CENTERS
NEWPORT

20050803 236

Naval Undersea Warfare Center Division
Newport, Rhode Island

PREFACE

Reviewed and Approved: 25 April 2005

Gerald M. Exley
Head, Communications, Imaging, and
EW Sensors Department

REPORT DOCUMENTATION PAGE

Public reporting for this collection of information is estimated to average 1 hour per response, including the time for reviewing instructions, searching existing data sources, gathering and maintaining the data needed, and completing and reviewing the collection of information. Send comments regarding this burden estimate or any other aspect of this collection of information, including suggestions for reducing this burden, to Washington Headquarters Services, Directorate for Information Operations and Reports, 1215 Jefferson Davis Highway, Suite 1204, Arlington, VA 22202-4302, and to the Office of Management and Budget, Paperwork Reduction Project (0704-0188), Washington, DC 20503.

1. AGENCY USE ONLY (Leave blank)	2. REPORT DATE 25 April 2005	3. REPORT TYPE AND DATES COVERED

4. TITLE AND SUBTITLE

Overview of the Equatorial Electrojet and Related Ionospheric Current Systems

5. FUNDING NUMBERS

PR A590045

6. AUTHOR(S)

John P. Casey

7. PERFORMING ORGANIZATION NAME(S) AND ADDRESS(ES)

Naval Undersea Warfare Center Division
1176 Howell Street
Newport, RI 02841-1708

8. PERFORMING ORGANIZATION REPORT NUMBER

TR 11,676

9. SPONSORING/MONITORING AGENCY NAME(S) AND ADDRESS(ES)

Office of Naval Research (ONR 312)
Ballston Centre Tower One
800 North Quincy Street
Arlington VA 22217-5660

10. SPONSORING/MONITORING AGENCY REPORT NUMBER

11. SUPPLEMENTARY NOTES

12a. DISTRIBUTION/AVAILABILITY STATEMENT

Approved for public release; distribution is unlimited.

12b. DISTRIBUTION CODE

13. ABSTRACT (Maximum 200 words)

The equatorial electrojet (EEJ) is an intense electric current that flows in the ionosphere in a narrow zone above the magnetic dip equator during the daytime. The electrojet current produces a large enhancement of the surface component of the geomagnetic field at and in the vicinity of the dip equator. The EEJ is most intense around local noontime and appears to be more stable than other ionospheric current systems.

This report presents a brief overview of the characteristics of the EEJ, including its location, electron density profile, current distribution, and magnetic field. In addition, the diurnal and seasonal variations of the EEJ are discussed. The relationship of the EEJ to the worldwide dynamo current system is discussed, in addition to a comparison with the auroral electrojet (AEJ). A derivation of the EEJ current distribution is presented that is based on an anisotropic conductivity model of the ionosphere. A summary of several experiments involving the generation of low-frequency signals from a heated and modulated EEJ is also given. It is anticipated that this report will provide helpful background information to scientists and engineers engaged in the development of future experiments that involve the transmission of signals in the ELF and VLF frequency bands from a heated and modulated EEJ.

14. SUBJECT TERMS				15. NUMBER OF PAGES 80
Ionosphere	Dynamo Process	Dip Equator	Electric Current Density	
Pedersen Conductivity	Hall Conductivity	Cowling Conductivity	Geomagnetic Variation	
Geomagnetic Solar Quiet Daily Variation		Geomagnetic Lunar Quiet Daily Variation		16. PRICE CODE
Extremely Low Frequency (ELF)		Very Low Frequency (VLF)		

17. SECURITY CLASSIFICATION OF REPORT	18. SECURITY CLASSIFICATION OF THIS PAGE	19. SECURITY CLASSIFICATION OF ABSTRACT	20. LIMITATION OF ABSTRACT
Unclassified	Unclassified	Unclassified	SAR

NSN 7540-01-280-5500

Standard Form 298 (Rev. 2-89)
Prescribed by ANSI Std. Z39-18
298-102

TABLE OF CONTENTS

Section   **Page**

LIST OF ILLUSTRATIONS

LIST OF ILLUSTRATIONS (Cont'd)

LIST OF TABLES

OVERVIEW OF THE EQUATORIAL ELECTROJET AND RELATED IONOSPHERIC CURRENT SYSTEMS

1. INTRODUCTION

Egedal discovered the equatorial electrojet (EEJ) in 1947-1948 (references 1-2) as an electric current that flows in a narrow zone of approximately 600 km in width above the magnetic dip equator. This intense electric current, which in daytime flows in an eastward direction was named the "equatorial electrojet" by Chapman in 1951 (reference 3). The EEJ represents a rather large enhancement of the diurnal variation in the horizontal or surface component of the geomagnetic field at and in the vicinity of the dip equator. The dip equator differs from the geomagnetic and geographic equators and is defined as the line at which the angle of inclination I (or dip angle) of the geomagnetic field B_0 is zero. The EEJ is characterized by its very high current density and eastward flow along the dip equator during the daytime hours, especially around local noon. The high current density is primarily attributed to the horizontal geomagnetic field lines at these latitudes. Measurements of the EEJ parameters have been obtained from magnetometers placed on rockets, satellites, and the ground, as well as from radar backscatter experiments.

The purpose of this report is to provide an overview of the characteristics of the EEJ, including its location, width, current distribution, magnetic field, and diurnal variation. The relationship of the EEJ to the worldwide dynamo current system is also discussed. A brief overview of the auroral electrojet (AEJ) is given and a comparison of the EEJ and AEJ current systems is presented. Finally, some experiments involved with the generation of low-frequency signals from a heated and modulated EEJ are summarized. A considerable number of theoretical and experimental investigations of the EEJ have been performed as evidenced by the large number of references that appear in the literature. Onwumechili's monograph (reference 4) provides an excellent overview of the EEJ and worldwide ionospheric current systems. Much of the information gathered for this report was obtained from Onwumechili's book and from various articles published in the *Journal of Geophysical Research* (see the list of references).

2. DESCRIPTION OF GEOMAGNETIC FIELD

Before proceeding with a discussion of the EEJ and other ionospheric current systems, it is important to describe the geomagnetic field. Within the earth, there exists a small solid inner core and an electrically conducting liquid outer core that is in steady thermal convective motion. It is believed that the rotation of the earth in combination with this convective motion generates the main part of the geomagnetic field via a dynamo-like mechanism (reference 4). Although the geomagnetic field has varied significantly over geological time scales, the changes in the main part of the geomagnetic field are slow, with time constants of tens to thousands of years (reference 5). Therefore, the geomagnetic field is customarily considered to be stationary.

A convenient analytical representation of the geomagnetic field is given in terms of a magnetic scalar potential Φ_m. Because the stationary currents that produce the main geomagnetic field $\boldsymbol{B}_0$ are negligible both on and above the surface of the earth, one has

$$\nabla \times \boldsymbol{B}_0 = 0. \tag{2-1}$$

Therefore, $\boldsymbol{B}_0$ can be expressed in terms of the gradient of the potential; i.e.,

$$\boldsymbol{B}_0 = -\nabla \Phi_m. \tag{2-2}$$

From Maxwell's equations,

$$\nabla \cdot \boldsymbol{B}_0 = 0. \tag{2-3}$$

The substitution of expression (2-3) into (2-2) shows that Φ_m satisfies Laplace's equations, viz.;

$$\nabla^2 \Phi_m = 0. \tag{2-4}$$

Consider a geographic spherical coordinate system (r, θ, φ) that is fixed with respect to the rotating earth and aligned with the axis of rotation as shown in figure 2-1. In this coordinate system, the earth is assumed to be spherical and r denotes the radial distance measured from the center of the earth, θ is the colatitude or polar angle that is measured with respect to the north

3

geographic pole, and φ is the east longitude measured from the Greenwich meridian. If the earth is approximated by a sphere of radius a, the magnetic scalar potential may be expanded in terms of spherical multipoles. A spherical multipole expansion solution of equation (2-4) that is valid for $r \geq a$ is given by (references 5 and 6)

$$\Phi_m(r,\theta,\varphi) = a \sum_{n=1}^{\infty} \left(\tfrac{a}{r}\right)^{n+1} \sum_{m=0}^{n} P_n^m(\cos\theta)\left[g_{nm}\cos m\varphi + h_{nm}\sin m\varphi\right], \qquad (2\text{-}5)$$

where g_{nm} and h_{nm} are constants, and $P_n^m(x)$ denotes the associated Legendre polynomial of the first kind of degree n and order m. Note that the above potential formula arises from currents internal to the earth and ignores any currents external to the earth.
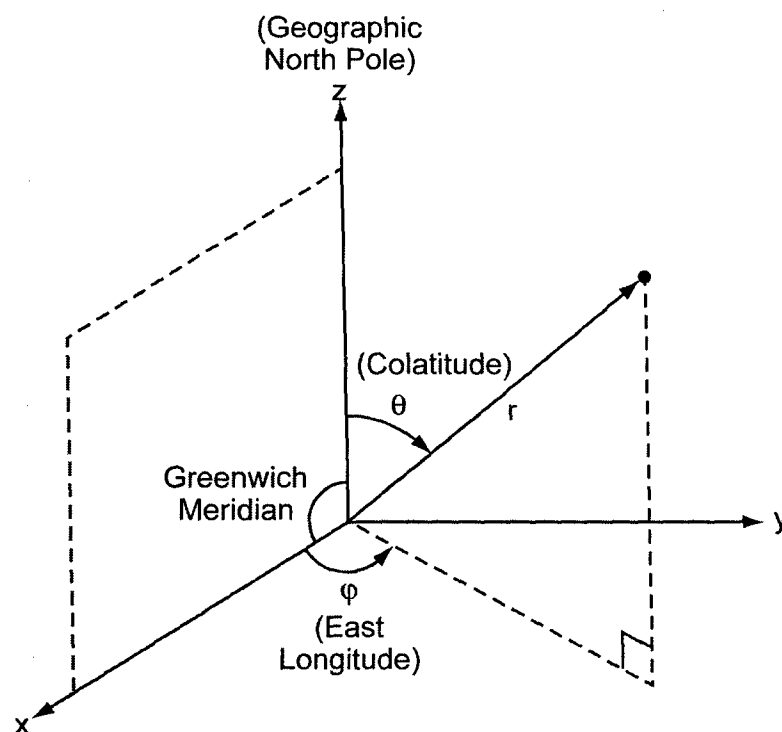
Figure 2-1. Geographic Coordinate System

A good approximation to expression (2-5) that accounts for 90% of the main geomagnetic field is given as the sum of the dipole ($n = 1$) terms; i.e.,

$$\Phi_m(r,\theta,\varphi) \cong a\left(\tfrac{a}{r}\right)^2 \left[g_{10}\cos\theta + \left(g_{11}\cos\varphi + h_{11}\sin\varphi\right)\sin\theta\right]. \qquad (2\text{-}6)$$

The above potential can be generated by three orthogonal magnetic dipoles located at the center of the earth, or equivalently, by a single magnetic dipole inclined at an angle α at the geographic pole given by (reference 6):

$$\alpha = \tan^{-1}\left[\sqrt{\frac{g_{11}^2 + h_{11}^2}{g_{10}^2}}\right].$$

(2-7)

For the earth, the single dipole equivalent is inclined at an angle of 11.5° to the axis of rotation toward 291.0° E (reference 5). Higher-order multipoles ($n > 1$) also contribute to the geomagnetic scalar potential Φ_m. However, the coefficients of the higher-order multipoles are much smaller in magnitude than the dipole coefficients and decrease rapidly with increasing n. The spherical harmonic coefficients for three different models of the geomagnetic field are listed in reference 5.

The geomagnetic field is given at any point in space by its direction and magnitude, which can be specified by the magnitudes of three orthogonal components, two direction angles and the magnitude, or some other set of three independent parameters. The components of the geomagnetic induction field along the geographic north, east, and vertical downward directions are denoted by X, Y, and Z, respectively, as illustrated in figure 2-2. From figure 2-2, these components are related to the geomagnetic field B_0 as follows:

$$X = B_0 \cos I \cos D = H \cos D ,$$

(2-8a)

$$Y = B_0 \cos I \sin D = H \sin D ,$$

(2-8b)

and

$$Z = B_0 \sin I ,$$

(2-8c)

where

$$H = B_0 \cos I = \sqrt{X^2 + Y^2} ,$$

(2-9)

and

$$B_0 = \sqrt{H^2 + Z^2} = \sqrt{X^2 + Y^2 + Z^2} .$$

(2-10)

In the above formulas, H is the horizontal component of the geomagnetic field, I is the dip angle, and D is the angle of declination. From formulas (2-8c) and (2-9), the dip angle is expressed in terms of the rectangular components as

$$I = \tan^{-1}\left(\frac{Z}{H}\right) = \tan^{-1}\left(\frac{Z}{\sqrt{X^2 + Y^2}}\right). \tag{2-11}$$

The dip angle is defined as positive when the geomagnetic field points downward and negative when the field points upward. In general, $I > 0$ in the northern magnetic hemisphere and $I < 0$ in the southern magnetic hemisphere. Note that H lies along the magnetic meridian, and the vertical plane through H is called the magnetic meridian plane (reference 4).
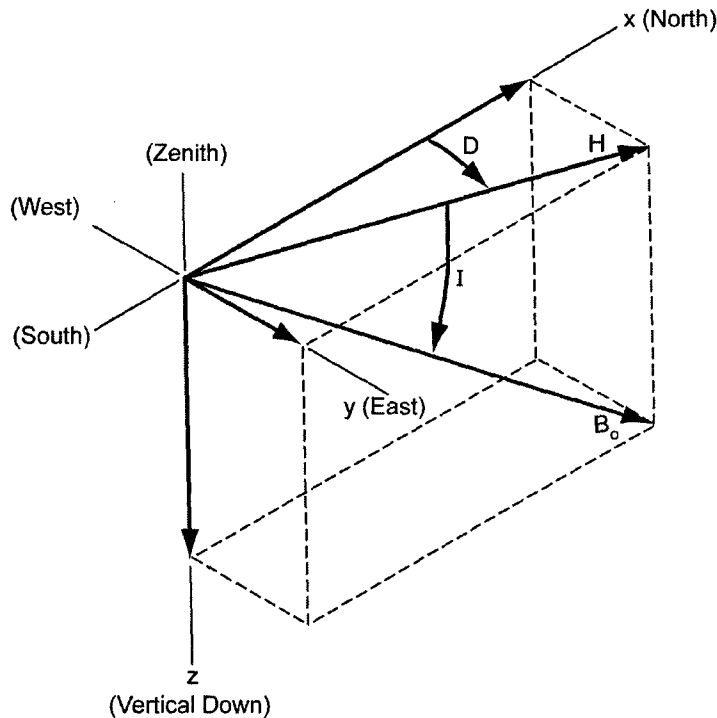
Figure 2-2. Definitions and Sign Conventions for Geomagnetic Field Components and Angles

Figure 2-3 describes some of the geomagnetic field parameters in the geographic vertical and horizontal planes. Particular combinations of three elements of the set $\{X, Y, Z, B_0, H, I, D\}$ can completely specify the geomagnetic field. The diurnal variations in the geomagnetic field components (X, Y, Z) associated with ionospheric currents are often expressed as $(\Delta X, \Delta Y, \Delta Z)$.

6

(a)
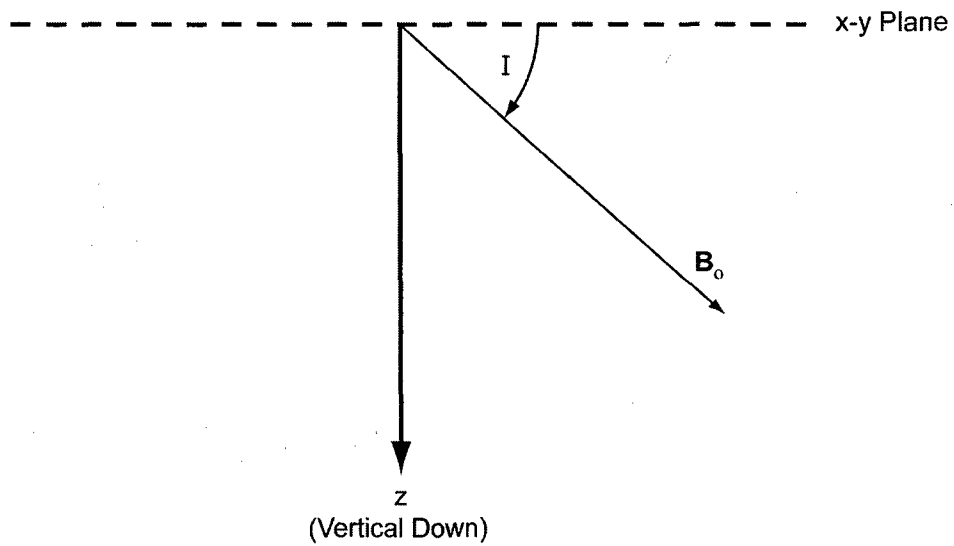
(b)
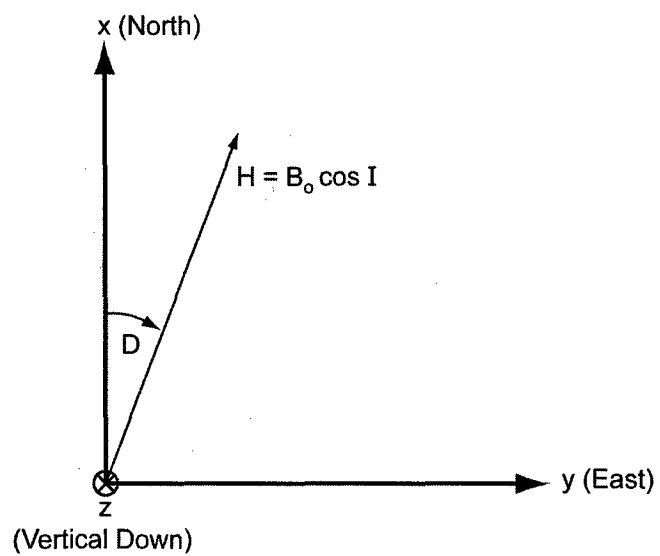
Figure 2-3. Coordinate System Used to Describe Geomagnetic Induction Field B$_o$: (a) Vertical Plane and (b) Horizontal Plane

Another coordinate system used to describe geomagnetic phenomena is the geomagnetic coordinate system $(r_m, \theta_m, \varphi_m)$ illustrated in figure 2-4. This is a spherical coordinate system that is fixed with respect to the earth with the polar axis inclined at 11.5° with respect to the axis of rotation and intersecting the earth's surface at 78.5° N latitude ($\theta = 11.5°$) and 291.0° E longitude. The geomagnetic polar axis corresponds to the axis of the magnetic dipole approximation to the geomagnetic field as described in formula (2-7). Because the equivalent magnetic dipole is located at the center of the earth, the coordinate r_m in the geomagnetic coordinate system is coincident with the coordinate r in the geographical coordinate system described in figure 2-1. The coordinate θ_m is the geomagnetic colatitude or polar angle that is measured with respect to the magnetic dipole axis, and φ_m is the geomagnetic longitude measured from the American half of the great circle, which passes through both the geographic and geomagnetic poles (reference 5). Therefore, the $\varphi_m = 0$ geomagnetic meridian is coincident with the 291.0° E longitude over most of its length (reference 5).
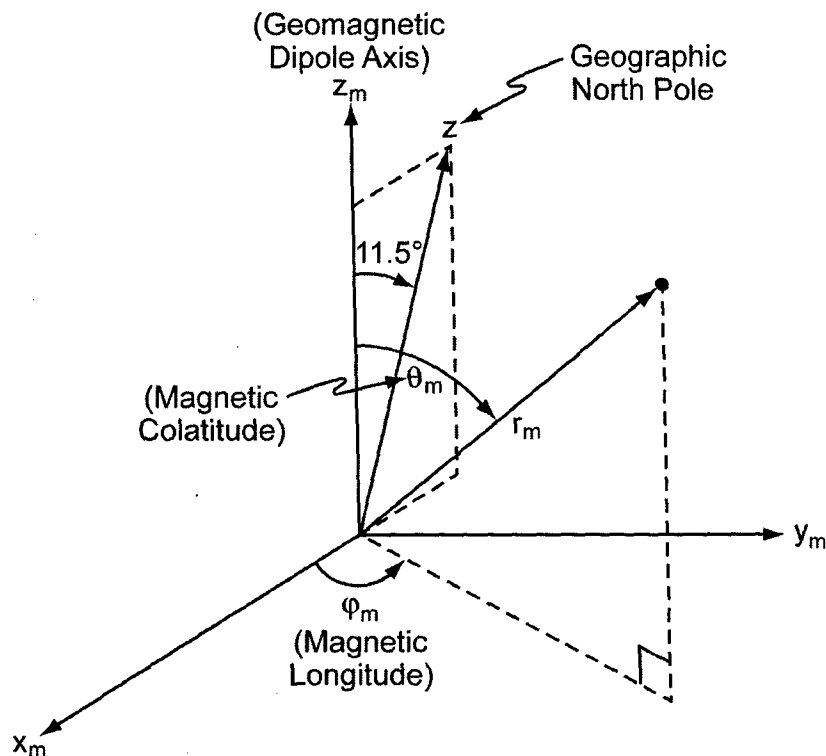
Figure 2-4. Geomagnetic Coordinate System

8

Figure 2-5 is a sketch of the geomagnetic field lines in the vicinity of the earth. In this illustration, N and S denote the geographic north and south poles, respectively, and B and A denote the boreal (north) and austral (south) geomagnetic poles, respectively. Note that the field lines point from south to north. Therefore, the magnetic dipole equivalent to the geomagnetic field is located at the center of the earth with its axis along the line AB and its positive end pointing toward A. At a distance of approximately 10 earth radii from the center of the earth, the interaction of the solar wind and interplanetary magnetic field (IMF) with the geomagnetic field results in a distortion of the geomagnetic field lines from those illustrated in figure 2-5 (reference 5).
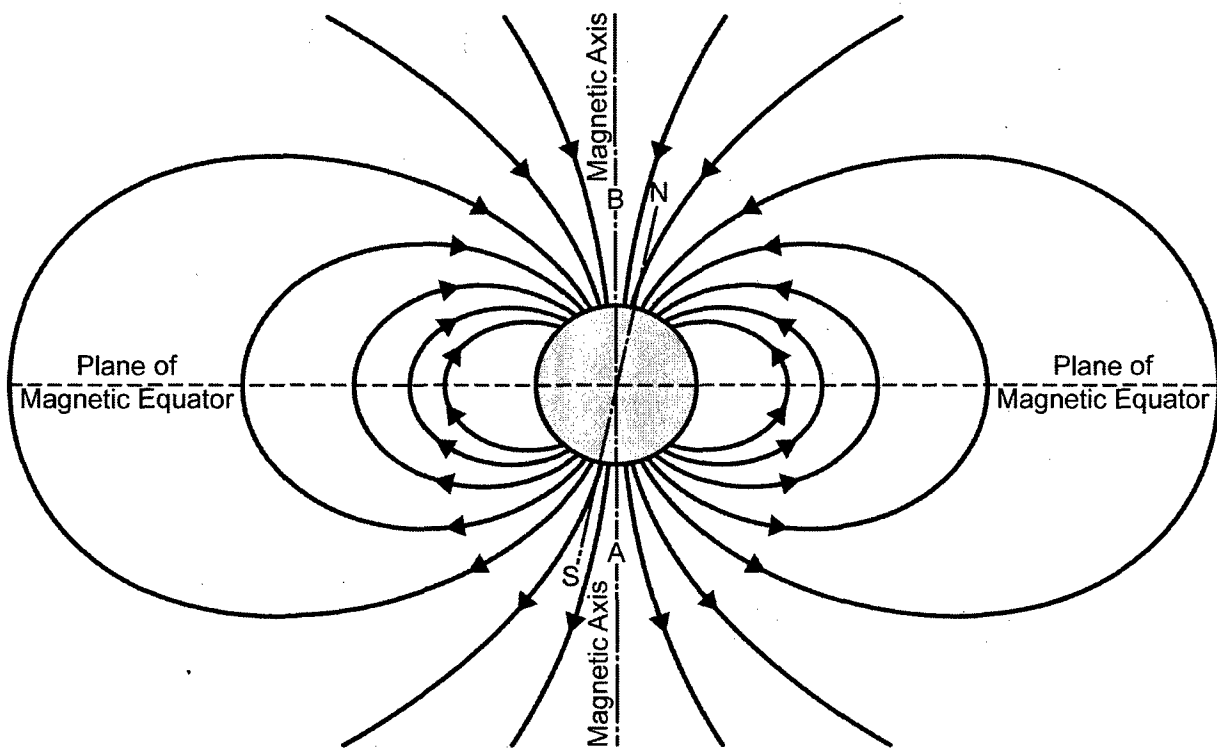
Figure 2-5. Geomagnetic Field Lines in the Vicinity of the Earth
(Taken from Onwumechili (reference 4), p. 2)

As mentioned, the EEJ is centered about the magnetic dip equator defined by $I = 0$. Therefore, the magnetic dip equator is very important in the description of the EEJ characteristics. The location of the EEJ center is most often represented by the dip latitude δ. The dip latitude is the distance in degrees latitude measured from the intersection of the magnetic dip equator and the geographic longitude of interest. Table 2-1 gives the 1968 and 1969 geographic latitude

coordinates where the magnetic dip equator crosses the meridians of longitude in intervals of 10°. This table also shows the variation in the geomagnetic field along the dip equator. The tabulated data show that the geomagnetic field is a maximum at 100° E longitude and a minimum at 300° E longitude. Because the ionospheric conductivity is inversely proportional to the geomagnetic field strength, the conductivity is a maximum at 300° E longitude and a minimum at 100° E longitude along the dip equator. Consequently, the EEJ is expected to be most intense at 300° E longitude (approximately 15° east of Huancayo, Peru) and least intense at 100° E (approximately 20° east of India). These observations are fairly consistent with measured data.

The variable δ is sometimes referred to as the "true" dip latitude (reference 4). Another measure of dip latitude L_d has been defined as

$$\tan L_d \equiv \frac{1}{2} \tan I = \frac{Z}{2H}.$$

(2-12)

Matsushita and Maeda (reference 7) used L_d to represent both the EEJ and upper ionospheric current layer, where H, Z, and I were measured values. L_d is a rough measure of dip latitude that distorts distances on the earth because of local magnetic anomalies and the nature of the graph of θ versus $\tan \theta$ (reference 4).

Figure 2-6 shows a world map with contours of constant inclination angle I as obtained from Knecht (reference 5). As previously mentioned, the EEJ center is located along the $I = 0$ contour. The contours in figure 2-6 were determined from the International Geomagnetic Reference Field (IGRF) for epoch 1965.0, a model based on a fit of formula (2-5) (with coefficients out to $n = m = 8$) to a weighted average of surface data obtained from observatories, land and sea surveys, aircraft, and satellites.

10

Table 2-1. Coordinates and Geomagnetic Induction Field B Where the Magnetic Dip Equator (I = 0) Crosses the Meridians of Longitude at Intervals of 10° in 1968 and 1969

(Taken from Onwumechili (reference 4), p. 9)

	1968			1969	
North Latitude Degree	East Longitude Degree	Intensity B nT	North Latitude Degree	East Longitude Degree	Intensity B nT
10.13	0	32389	10.17	0	32411
10.40	10	33422	10.42	10	33445
10.36	20	34441	10.40	20	34465
10.08	30	35307	10.08	30	35316
9.36	40	35958	9.36	40	35957
8.56	50	36645	8.56	50	36634
8.20	60	37687	8.20	60	37669
8.50	70	39032	8.52	70	39016
9.13	80	40254	9.16	80	40241
9.52	90	40969	9.52	90	40956
9.33	100	41028	9.33	100	41021
8.74	110	40514	8.74	110	40511
8.17	120	39620	8.17	120	39620
7.86	130	38476	7.86	130	38475
7.67	140	37159	7.71	140	37150
7.30	150	35857	7.35	150	35842
6.30	160	34900	6.35	160	34882
4.50	170	34479	4.50	170	34471
2.05	180	34435	2.29	180	34368
0.35	190	34201	0.38	190	34173
−0.90	200	33782	−0.90	200	33753
−1.80	210	33272	−1.81	210	33242
−2.62	220	32776	−2.65	220	32743
−3.50	230	32311	−3.50	230	32274
−4.35	240	31886	−4.35	240	31846
−5.45	250	31456	−5.47	250	31410
−7.15	260	30838	−7.16	260	30786
−9.50	270	29822	−9.53	270	29759
−12.05	280	28382	−12.05	280	28318
−13.78	290	26868	−13.74	290	26811
−13.39	300	25962	−13.33	300	25911
−10.29	310	26092	−10.17	310	26062
−4.89	320	27117	−4.72	320	27112
1.37	330	28633	1.53	330	28639
6.29	340	30121	6.43	340	30139
9.04	350	31345	9.13	350	31367
10.13	360	32389	10.17	360	32411
Mean		33818			33800
Standard Deviation		4311			4320
Median		34321			33344
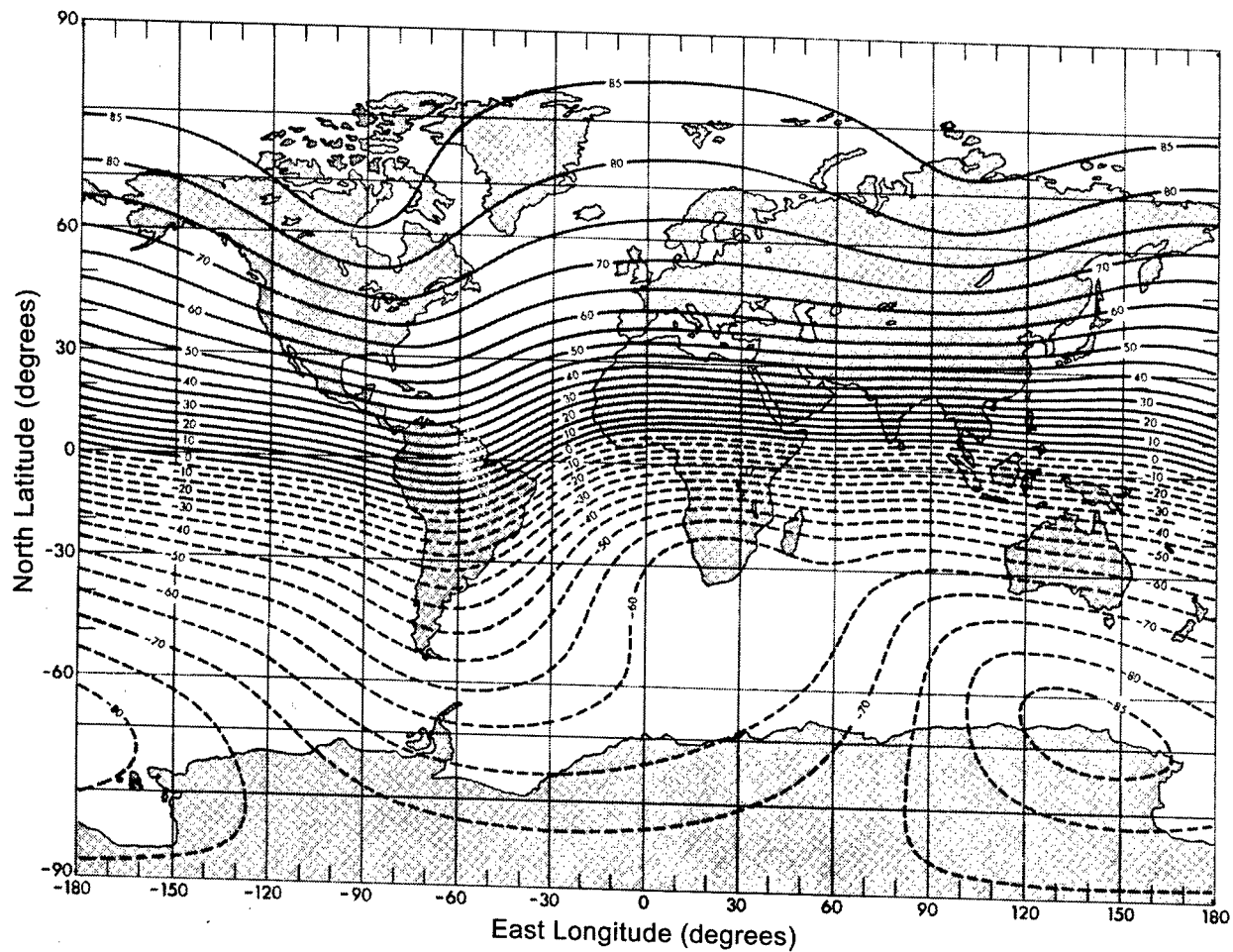
Figure 2-6. Contours of Constant Dip Angle I for the International Geomagnetic Reference Field for Epoch 1965.0
(Taken from Knecht (reference 5), p. 50)

3. EQUATORIAL ELECTROJET

The sun and the moon produce tidal forces in the atmosphere, which result in air motion that is primarily horizontal. The motion of the air across the geomagnetic field induces electromotive forces, which drive electric currents at altitudes in the ionosphere where the air is electrically conducting, causing daily variations in the geomagnetic field. This has been referred to as the atmospheric dynamo theory (references 4 and 6). Solar particles emitted from the sun also interact with the magnetosphere of the earth to produce additional perturbations in the geomagnetic field, referred to as geomagnetic disturbance. On a quiet day when the geomagnetic disturbance is negligible, the dominant part of the observed geomagnetic variation is a function of solar time, referred to as the geomagnetic solar quiet daily variation Sq; and the minor part is a function of lunar time, called the geomagnetic lunar quiet daily variation L. The ionospheric currents associated with L contribute only about 5% to the normal variation in the geomagnetic field. Because L is very small, it is difficult to extract from the observed geomagnetic daily variation.

Ionospheric current systems, including the EEJ, are the result of the above dynamo process. In the ionosphere, the conducting particles (electrons and ions) move at a velocity v in the presence of the stationary geomagnetic induction field B_0, resulting in an induced electromotive force (EMF) of $v \times B_0$ on the particles. This induced electric field $v \times B_0$ results in the flow of current in the ionosphere. The resulting dynamo currents occur primarily in the E-region of the ionosphere (90- to 150-km altitude range), where the electrical conductivity is appreciable.

3.1 CONDUCTIVITY MODEL OF THE EQUATORIAL IONOSPHERE

Consider the general case in which an applied electric field E is neither parallel nor perpendicular to the geomagnetic field B_0. The current density J is related to the electric field through the following general formula:

$$J = \bar{\sigma} \cdot E, \tag{3-1}$$

where $\bar{\sigma}$ is the conductivity tensor that is expressed in matrix form as

$$\bar{\sigma} = \begin{bmatrix} \sigma_{xx} & \sigma_{xy} & \sigma_{xz} \\ \sigma_{yx} & \sigma_{yy} & \sigma_{yz} \\ \sigma_{zx} & \sigma_{zy} & \sigma_{zz} \end{bmatrix} , \tag{3-2}$$

and E is given by

$$E = u_x E_x + u_y E_y + u_z E_z . \tag{3-3}$$

In the above expressions, the coordinates are defined with respect to the magnetic meridian (x, z) plane, where the x-, y-, and z-coordinates refer to the magnetic north, magnetic east, and vertical-downward directions, respectively. In addition, u_x, u_y, and u_z denote the unit vectors along the x-, y-, and z-directions, respectively. The geomagnetic induction field B_0 is given by

$$B_0 = u_\parallel |B_0| = u_\parallel B_0 , \tag{3-4}$$

where $u_\parallel$ is a unit vector parallel to B_0 and is expressed as

$$u_\parallel = u_x \cos I + u_z \sin I . \tag{3-5}$$

Note that I is the dip angle of B_0. The unit vector $u_\perp$ lies in the magnetic meridian plane, perpendicular to B_0, and is given by

$$u_\perp = - u_x \sin I + u_z \cos I . \tag{3-6}$$

The unit vectors $u_\parallel$ and $u_\perp$ are illustrated in figure 3-1.

14
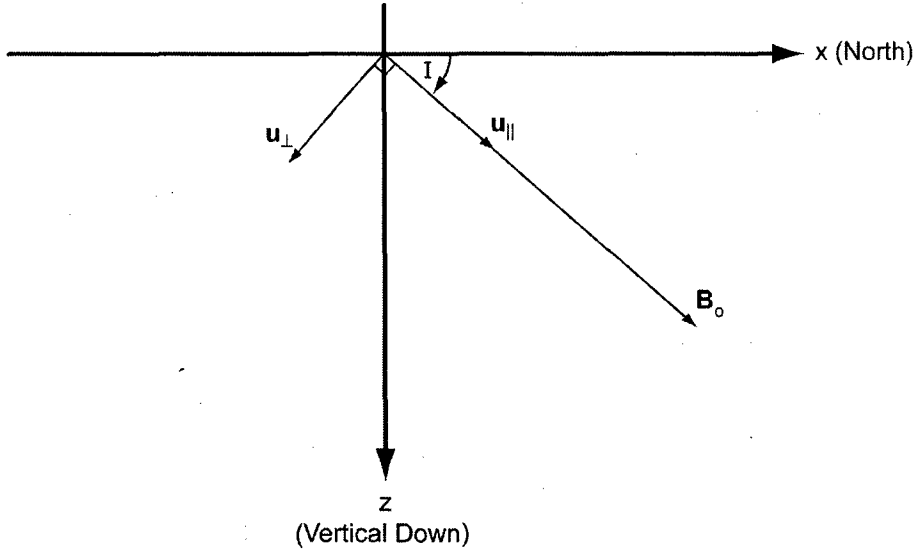
Figure 3-1. Magnetic Meridian Plane with Unit Vectors $u_{\parallel}$ and $u_{\perp}$ Directed Parallel and Perpendicular to Geomagnetic Field B_o

The ionospheric current density is given as the sum of three components (references 4 and 6):

$$J = \sigma_{\parallel} E_{\parallel} + \sigma_p E_{\perp} + \sigma_h\, u_{\parallel} \times E \; , \qquad (3\text{-}7)$$

where $\sigma_{\parallel} E_{\parallel}$, $\sigma_p E_{\perp}$, and $\sigma_h\, u_{\parallel} \times E$ denote the parallel, Pedersen, and Hall currents, respectively. The terms $\sigma_{\parallel}$, σ_p, and σ_h refer to the parallel, Pedersen, and Hall conductivities, respectively, and are given by (references 4 and 6)

$$\sigma_{\parallel} = \frac{ne^2}{mv} = \frac{|e|n\omega_c}{B_o v} \; , \qquad (3\text{-}8a)$$

$$\sigma_p = \sigma_{\parallel}\left(\frac{v^2}{v^2 + \omega_c^2}\right) \; , \qquad (3\text{-}8b)$$

and

$$\sigma_h = \sigma_{\parallel}\left(\frac{v\omega_c}{v^2 + \omega_c^2}\right) , \qquad (3\text{-}8c)$$

where n is the number density, e is the charge, m is the mass of the particle, v denotes the collision frequency, and ω_c is the cyclotron angular frequency given by

15

$$\omega_c = \frac{|e| B_o}{m} \ . \tag{3-9}$$

Note that n, e, m, v, and ω_c depend on the particle type (i.e., electron, positive ion, or negative ion). Therefore, the conductivities in formulas (3-8) must each be expressed as a sum over the particle types.

In the ionosphere, neutral particles are generally much greater in number than charged particles. Consequently, collisions with neutral particles have a large influence on the conductivity values given in expressions (3-8). Following Onwumechili (reference 4), let v_e, v_+, and v_- denote the effective collision frequencies of electrons, positive ions, and negative ions, respectively, with all particle types. Similarly, the effective masses are denoted by m_e, m_+, and m_-, and the corresponding cyclotron frequencies by ω_{ce}, ω_{c+}, and ω_{c-}. If the conductivities given in formulas (3-8) are each summed over the three charged particle types, they become

$$\sigma_{\parallel} = e^2 \left(\frac{n_e}{m_e v_e} + \frac{n_+}{m_+ v_+} + \frac{n_-}{m_- v_-} \right) = \frac{|e|}{B_o} \left(\frac{n_e \omega_{ce}}{v_e} + \frac{n_+ \omega_{c+}}{v_+} + \frac{n_- \omega_{c-}}{v_-} \right), \tag{3-10a}$$

$$\sigma_p = \sigma_{\parallel} \left(\frac{v_e^2}{v_e^2 + \omega_{ce}^2} + \frac{v_+^2}{v_+^2 + \omega_{c+}^2} + \frac{v_-^2}{v_-^2 + \omega_{c-}^2} \right), \tag{3-10b}$$

and

$$\sigma_h = \sigma_{\parallel} \left(\frac{v_e \omega_{ce}}{v_e^2 + \omega_{ce}^2} + \frac{v_+ \omega_{c+}}{v_+^2 + \omega_{c+}^2} + \frac{v_- \omega_{c-}}{v_-^2 + \omega_{c-}^2} \right). \tag{3-10c}$$

Note that the above formulas apply at zero frequency. The more-general frequency-dependent conductivity formulas (unnecessary for the present application) are given in Ishimaru's text (reference 8).

In formula (3-7) for the ionospheric current density, $E_{\parallel}$ is the electric field parallel to B_o, $E_\perp$ is the component of E that is perpendicular to B_o and lies in the magnetic meridian (x, z) plane, and $u_{\parallel} \times E$ is the perpendicular to both E and B_o. From expressions (3-3), (3-5), and (3-6), these quantities are given as follows:

$$E_{\parallel} = u_{\parallel} \, (E \cdot u_{\parallel})$$

$$= u_x \left(E_x \cos^2 I + E_z \cos I \sin I \right) + u_z \left(E_x \cos I \sin I + E_z \sin^2 I \right) , \qquad (3\text{-}11)$$

$$E_{\perp} = u_{\perp} \, (E \cdot u_{\perp}) + u_y \, E_y$$

$$= u_x \left(E_x \sin^2 I - E_z \cos I \sin I \right) + u_y \, E_y + u_z \left(-E_x \cos I \sin I + E_z \cos^2 I \right) , \quad (3\text{-}12)$$

$$u_{\parallel} \times E = -\, u_x \, E_y \sin I + u_y \left(E_x \sin I - E_z \cos I \right) + u_z \, E_y \cos I \cdot \qquad (3\text{-}13)$$

The substitution of the above formulas into the current density expression yields

$$J = u_x \left[\left(\sigma_{\parallel} \cos^2 I + \sigma_p \sin^2 I \right) E_x - \sigma_h \sin I \, E_y + (\sigma_{\parallel} - \sigma_p) \cos I \sin I \, E_z \right]$$

$$+ u_y \left[\sigma_h \sin I \, E_x + \sigma_p \, E_y - \sigma_h \cos I \, E_z \right]$$

$$+ u_z \left[(\sigma_{\parallel} - \sigma_p) \cos I \sin I \, E_x + \sigma_h \cos I \, E_y + \left(\sigma_{\parallel} \sin^2 I + \sigma_p \cos^2 I \right) E_z \right]. \quad (3\text{-}14)$$

A comparison of formulas (3-1) and (3-2) with (3-14) yields the following expressions for the elements of the conductivity tensor:

$$\sigma_{xx} = \sigma_{\parallel} \cos^2 I + \sigma_p \sin^2 I , \qquad\qquad (3\text{-}15a)$$

$$\sigma_{xy} = -\, \sigma_{yx} = -\, \sigma_h \sin I , \qquad\qquad (3\text{-}15b)$$

$$\sigma_{xz} = \sigma_{zx} = (\sigma_{\parallel} - \sigma_p) \cos I \sin I , \qquad\qquad (3\text{-}15c)$$

$$\sigma_{yy} = \sigma_p , \qquad\qquad (3\text{-}15d)$$

$$\sigma_{yz} = -\, \sigma_{zy} = -\, \sigma_h \cos I , \qquad\qquad (3\text{-}15e)$$

$$\sigma_{zz} = \sigma_{\parallel} \sin^2 I + \sigma_p \cos^2 I . \qquad\qquad (3\text{-}15f)$$

The ionospheric conductivity is anisotropic because of the presence of the geomagnetic field $\boldsymbol{B_0}$. In addition, the conductivity components vary with altitude along with the latitude and longitude coordinates.

A popular assumption made by many investigators is to assume that no vertical current flows (i.e., $J_z = 0$). If the z component of current density in formula (3-14) is set to zero, the vertical electric field is

$$E_z = \frac{-(\sigma_{\parallel} - \sigma_p) \cos I \sin I \, E_x - \sigma_h \cos I \, E_y}{\sigma_{\parallel} \sin^2 I + \sigma_p \cos^2 I} . \qquad (3\text{-}16)$$

The substitution of expression (3-16) into the x and y components of current density in expression (3-14) yields

$$J_x = \sigma_{xx} E_x + \sigma_{xy} E_y , \qquad (3\text{-}17a)$$

and

$$J_y = -\sigma_{xy} E_x + \sigma_{yy} E_y , \qquad (3\text{-}17b)$$

where the conductivity components are

$$\sigma_{xx} = \frac{\sigma_{\parallel} \sigma_p}{\sigma_{\parallel} \sin^2 I + \sigma_p \cos^2 I} , \qquad (3\text{-}18a)$$

$$\sigma_{xy} = -\sigma_{yx} = \frac{-\sigma_{\parallel} \sigma_h \sin I}{\sigma_{\parallel} \sin^2 I + \sigma_p \cos^2 I} , \qquad (3\text{-}18b)$$

$$\sigma_{yy} = \frac{\sigma_{\parallel} \sigma_p \sin^2 I + (\sigma_p^2 + \sigma_h^2) \cos^2 I}{\sigma_{\parallel} \sin^2 I + \sigma_p \cos^2 I} . \qquad (3\text{-}18c)$$

Onwumechili (reference 4) refers to the above tensor elements as the layer conductivities.

At the geomagnetic dip equator, where the dip angle $I = 0$, the conductivities in expressions (3-18) reduce to

18

$$\sigma_{xx} = \sigma_{\parallel}, \tag{3-19a}$$

$$\sigma_{xy} = \sigma_{yx} = 0, \tag{3-19b}$$

and

$$\sigma_{yy} = \sigma_p + \frac{\sigma_h^2}{\sigma_p} \equiv \sigma_c. \tag{3-19c}$$

In expression (3-19c), σ_c is referred to as the Cowling conductivity (references 4 and 6). The Cowling conductivity is the effective conductivity of the EEJ that flows along the y or eastward direction at and in the vicinity of the dip equator. Figure 3-2 shows the electron density n_e, the ratio of Hall to Pedersen conductivities (σ_h/σ_p), the Cowling conductivity, and the EEJ current density each as functions of altitude in the vicinity of the dip equator as obtained from rocket measurements reported by Subbaraya et al. (reference 9). The electron density profile was measured at 10:40 AM local time (LT) on 28 January 1971, and the current density was measured at 11:08 AM LT on 29 August 1968. The conductivities were determined from the electron density measurements. The plots show that each quantity increases with altitude, with the ratio σ_h/σ_p reaching its peak of about 28 at approximately 97 km, σ_c peaking at 0.014 S/m at approximately 102 km, and the current density peaking at about 105 km at a magnitude of 9.4 A/km². The Cowling conductivity reaches a peak at approximately 5 km beyond the peak of σ_h/σ_p because the Hall conductivity continues to increase with altitude just beyond 97 km. The EEJ current is a maximum at an altitude of several km above that of the Cowling conductivity peak because of the continued increase of the east-west electrostatic field E_y with altitude (figure 3-3). These plots are typical of other measurements made in the vicinity of the dip equator.

Figure 3-3 shows that at an altitude of 110 km the east-west electrostatic field decreased significantly at 1345 hr and 1415 hr from its earlier value of approximately 1.1 mV/m at 1017 hr. From comparisons of measured data, Subbaraya et al. (reference 9) observed that at about 1330 to 1400 hr LT, the EEJ current had decreased to about half of its maximum value at local noon. Subbaraya et al. attributed this decrease in current to a decrease in the east-west electrostatic field and not to the electron density or the conductivity.

Figure 3-2 shows that the electron density reaches a maximum at several kilometers above the peak of the EEJ current density. After reaching this local maximum, the electron density decreases with altitude over a short distance and then increases with altitude throughout the remainder of the E-region. The current density can be expressed as

$$J = en_e v ,$$ (3-20)

where v is the electron streaming velocity (reference 4). Because figure 3-2 shows that n_e continues to increase with altitude after the EEJ current reaches a maximum, the above current density formula indicates that v decreases much faster with altitude than J for heights above the peak value of J.
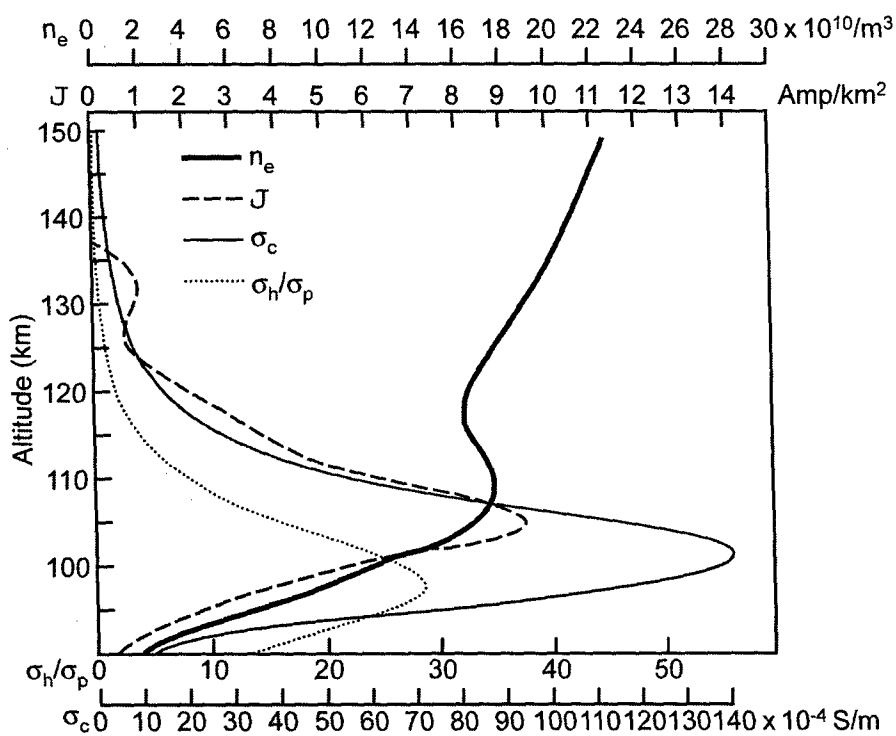
Figure 3-2. *Altitude Profiles of the Electron Density (n_e), Ratio of Hall-to-Pedersen Conductivities (σ_h/σ_p), Cowling Conductivity (σ_c), and Current Density J Obtained from Rocket Measurements Made Above Thumba, India, at –0.47° Dip Latitude, as Reported by Subbaraya et al. (Reference 9)*
(Taken from Onwumechili (reference 4), p. 124.)
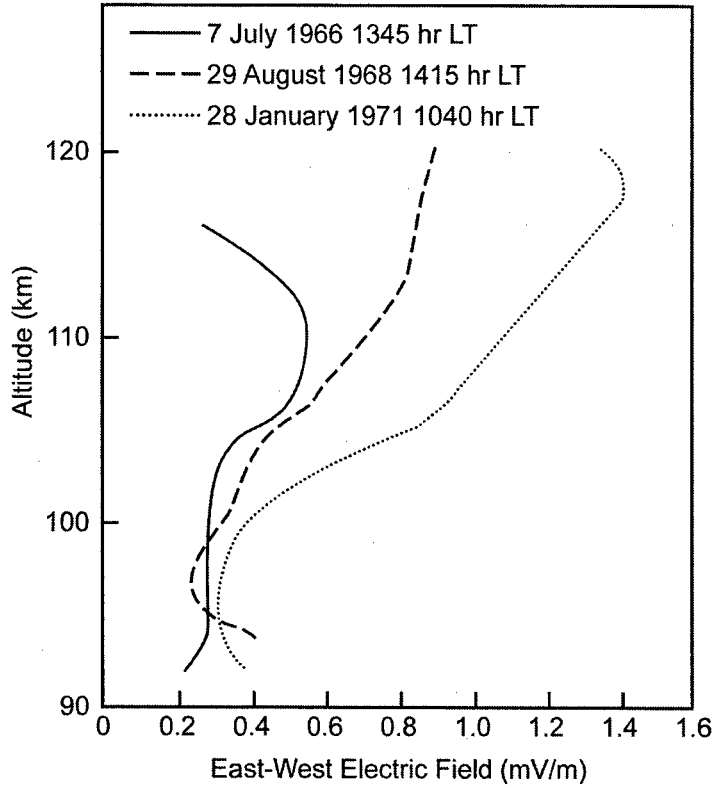
***Figure 3-3. East-West Component of Electrostatic Electric Field vs Altitude, Calculated from
Electrical Conductivity and Electric Currents Obtained from Rocket Measurements Made
Above Thumba, India, at − 0.47° Dip Latitude, as Reported by Subbaraya et al. (Reference 9)***
(Taken from Onwumechili (reference 4), p. 125)

Figure 3-4 shows plots of the conductivities $\sigma_{\parallel}$, σ_p, σ_h, and σ_c computed by Forbes and

Lindzen (reference 10) as a function of altitude under noontime equatorial, equinox, and average

solar conditions. The plots show that the parallel conductivity is approximately four orders of

magnitude greater than the Pedersen and Hall conductivities. From these plots, the peak values

of σ_p, σ_h, and σ_c are 6.3 x 10^{-4} S/m, 8.5 x 10^{-4} S/m, and 0.018 S/m, respectively, at heights of

130 km, 114 km, and 102 km, respectively. As shown in figure 3-2, the EEJ current is a

maximum at an altitude of about 105 km. Therefore, the plots in figure 3-4 suggest that a large

Hall current drives the EEJ. In the evening, conductivities (including the ratio σ_h/σ_p) decrease

significantly from their midday values. Therefore, it is not surprising that the EEJ does not exist

at nighttime.
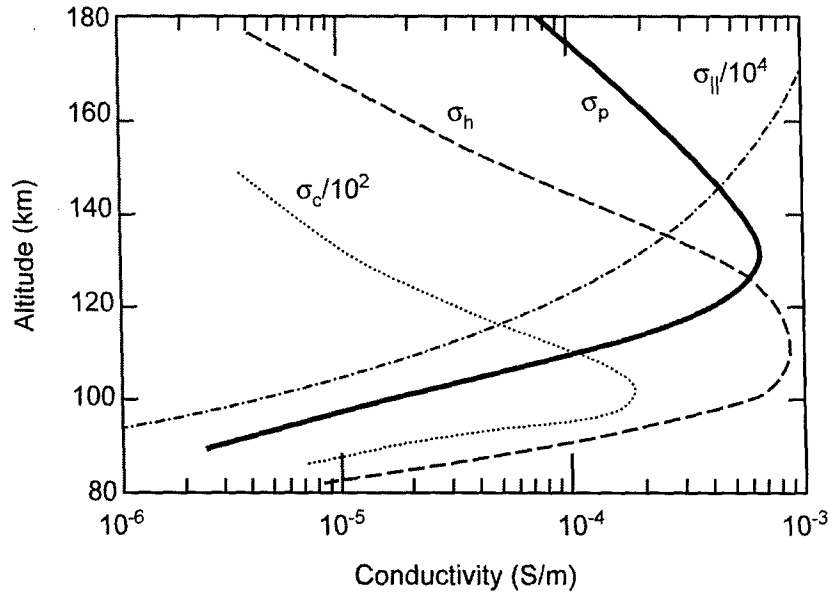
***Figure 3-4. Parallel (σ_0), Pedersen (σ_1), Hall (σ_2), and Cowling (σ_3) Conductivities
as a Function of Height Under Noontime Equatorial, Equinox, and
Average Solar Conditions, as Reported by Forbes and Lindzen (Reference 10)***
(Taken from Onwumechili (reference 4), p. 162)

Formulas (3-16) through (3-19) are based on the assumption that no vertical current flows
($J_z = 0$); i.e., all current flows in a thin ionospheric shell at a given height. Under this
assumption, the vertical component of the wind velocity is ignored, and the current density and
conductivity tensor are each integrated with respect to altitude and assumed to exist in a
spherical shell. The height-integrated current density J_s (A/m) is

$$J_s = \int J \, dz, \tag{3-21}$$

where the integration is performed over the altitude range of the current, a region of high
conductivity. From expression (3-1), J_s is related to the electric field E by

$$J_s = \bar{\Sigma} \cdot E, \tag{3-22}$$

where $\bar{\Sigma}$ is the height-integrated conductivity tensor with Cartesian components given by

22

$$\Sigma_{xx} = \int \sigma_{xx}\, dz, \qquad\qquad (3\text{-}23a)$$

$$\Sigma_{xy} = \int \sigma_{xy}\, dz, \qquad\qquad (3\text{-}23b)$$

and

$$\Sigma_{yy} = \int \sigma_{yy}\, dz. \qquad\qquad (3\text{-}23c)$$

Note that the units of $\bar{\Sigma}$ are mhos ($\mho$) or siemens (S). In expression (3-22), E is the average value of electric field (with respect to altitude) within the highly conducting layer. Table 3-1 lists the components of the height-integrated conductivity tensor as a function of dip latitude as determined by Matsushita (reference 11). This table shows that the diagonal components Σ_{xx} and Σ_{yy} are each at a maximum along the dip equator and decrease with increasing dip latitude. The off-diagonal component Σ_{xy} vanishes at the dip equator, is a maximum just beyond the dip equator, and then decreases with increasing dip latitude. Along the dip equator, formulas (3-19) and (3-23) indicate that Σ_{xx} and Σ_{yy} are the height-integrated parallel and Cowling conductivities, respectively.

Table 3-1. Height-Integrated Conductivities at Different Latitudes at Local Noon as Obtained from Matsushita (Reference 11)

Dip Latitude (deg)	Σ_{xx} (mhos)	Σ_{xy} (mhos)	Σ_{yy} (mhos)
0	1.07×10^5	0	250.0
1	1.03×10^4	588.0	52.8
2	2.83×10^3	331.0	25.8
3	1.28×10^3	225.0	19.5
6	324	112.0	15.1
9	145	73.0	13.8
12	82.8	53.4	13.0
15	54.0	41.5	12.2
21	28.9	27.9	10.8
30	15.5	17.8	8.90
45	8.14	10.3	6.52
60	5.41	6.91	4.99
75	4.27	5.38	4.19
90	4.05	5.12	4.05

3.2 PHYSICAL BASIS FOR THE EEJ AND WSq CURRENTS IN
THE DIP EQUATORIAL REGION

In the dip equatorial zone, the geomagnetic field B_0 is horizontal and directed northward while the zonal component of the electrostatic polarization field E_{zon} produced by global dynamo action is directed eastward during the daytime and is nearly constant in latitude, but increases somewhat as a function of height in the dynamo region (90–150 km) as shown in figure 3-3. The crossed electric and magnetic fields cause the electrons and ions to drift at a velocity v_d given by (reference 12)

$$v_d = \frac{E_{zon} \times B_0}{|B_0|^2},$$

(3-24)

where v_d is directed vertically upward. As a result, Hall current $\sigma_h\, u_{\parallel} \times E_{zon}$ flows downward (see the coordinate system in figure 3-1). In the altitude range 70–130 km, $v_e < \omega_{ce}$ and $v_i > \omega_{ci}$, where the subscripts e and i refer to electrons and ions, respectively. As a result, the electrons move upward, while the ions are restrained from moving because of collisions. Because $v_e = \omega_{ce}$ at an altitude of approximately 70 km and $v_i = \omega_{ci}$ at a height of about 130 km, the ionosphere is a poor conductor at these altitudes and the Hall current is impeded. Consequently, charges accumulate at these two altitudes (figure 3-5) and an upward polarization electric field given by

$$E_h = \frac{\sigma_h}{\sigma_p} (E_{zon} \times u_{\parallel})$$

(3-25)

is created if vertical current is inhibited (reference 4). E_h is referred to as the Hall polarization electric field.

The Hall current, given by $\sigma_h\, u_{\parallel} \times E$ in equation (3-7), is perpendicular to both the electric and geomagnetic fields. Therefore, because the vertical Hall polarization electric field is perpendicular to the horizontal northward geomagnetic field at the dip equator, another Hall current J_h is produced and is given by

$$J_h = \sigma_h\, u_{\parallel} \times E_h.$$

(3-26)

Note that J_h is along the eastward direction. Because the Hall conductivity σ_h is a maximum at an altitude of approximately 110 km, J_h is also a maximum at that height.
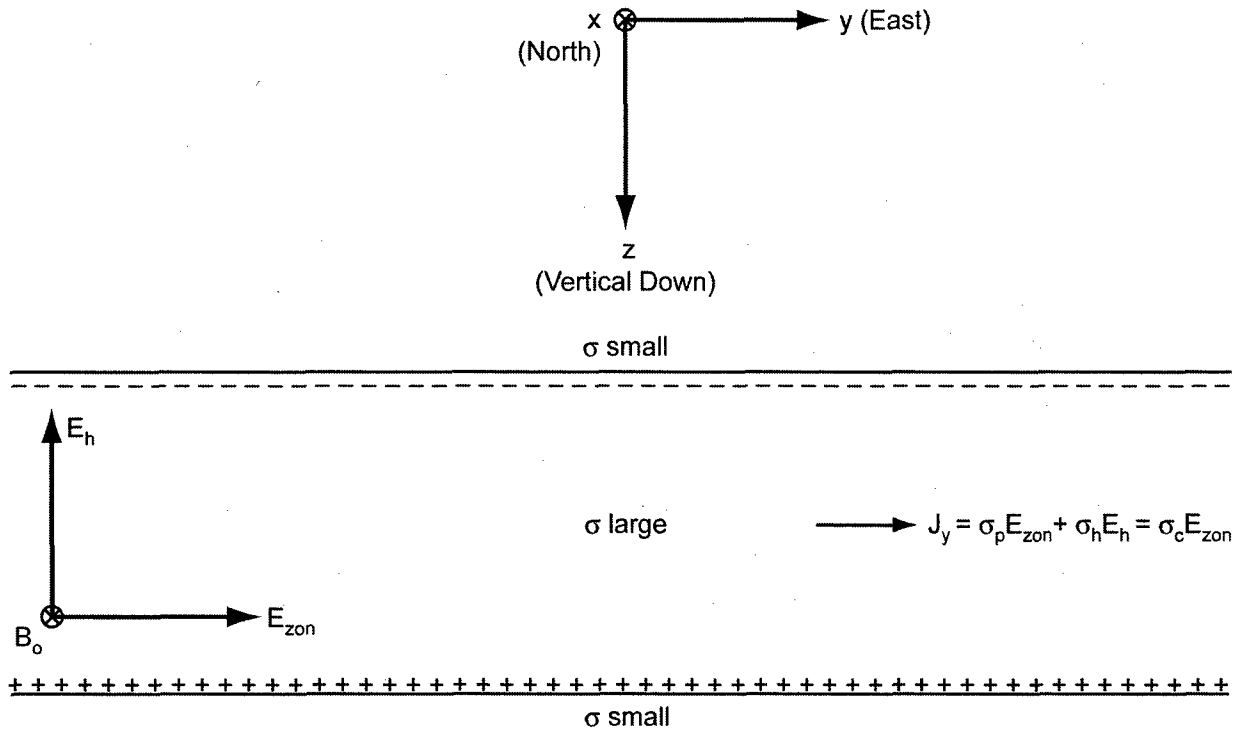
Figure 3-5. Electric Field and Current Structure in Dip Equatorial Region

At the dip equator, the total current density is given by

$$J = J_h + J_p ,$$ (3-27)

where J_p is the Pedersen current,

$$J_p = \sigma_p E_{zon} = u_y \, \sigma_p \, |E_{zon}| .$$ (3-28)

(Refer to figure 3-5.) The substitution of formulas (3-25), (3-26), and (3-28) into (3-27) yields

$$J = \frac{\sigma_h^2}{\sigma_p} \left[u_{\parallel} \times \left(E_{zon} \times u_{\parallel} \right) \right] + \sigma_p E_{zon} = \left(\sigma_p + \frac{\sigma_h^2}{\sigma_p} \right) E_{zon} = u_y \, \sigma_c \, |E_{zon}| ,$$ (3-29)

where σ_c is the Cowling conductivity defined in expression (3-19c). Note that formula (3-29) is the same result as derived in section 3.1. The above expression shows that σ_c is the effective conductivity at the dip equator. Onwumechili (reference 4) states that E_h is more than 20 times greater in magnitude than E_{zon} at altitudes near 110 km. Because $\sigma_h \gg \sigma_p$ in the vicinity of 110 km, the current in this altitude range is predominantly Hall current. Therefore, this analysis

shows that a Hall current that travels along the eastward direction at an altitude of approximately 110 km drives the EEJ. Rocket measurements have shown that the EEJ peaks at an altitude of 106.4 ± 0.6 km (reference 4).

In the EEJ region, Onwumechili (reference 4) states that, in addition to the zonal electric field E_{zon} and Hall electric field E_h, there is a local vertical field E_L associated with the local zonal winds with vertical shear. However, E_L is quite small near the dip equator and can be neglected. Over much of the dynamo region, $|E_{zon}|$ is approximately 0.5 mV/m (see figure 3-3). The Pedersen conductivity is a maximum at an altitude of about 130 km (see figure 3-4). Because $\sigma_h/\sigma_p \approx 0.5$ and $|E_h|/|E_{zon}| \approx 0.5$ at 130 km, the Pedersen current is approximately four times greater than the Hall current at this altitude. Therefore, a second upper current layer exists at this higher altitude that is a predominantly Pedersen current. This upper current layer can be seen in the measured current distribution shown in figure 3-2, which illustrates a secondary peak in the current density at an altitude of 132 km. Note that the upper current layer is much smaller in magnitude than the EEJ (or lower current layer) that is centered at an altitude of approximately 105 km. Onwumechili (reference 4) has associated this upper ionospheric current layer with the worldwide part of the Sq current systems (often referred to as WSq currents). Onwumechili (reference 4) states that within $\pm 2°$ dip latitude, this upper current layer peaks at an altitude of 136 ± 8 km. (The WSq current system will be defined in section 4.)

Figure 3-6 shows an altitude profile of the vertical electric field $E_z = E_h$ measured by Sartiel (reference 13) near the dip equator during a moderate EEJ. The curve shows a maximum field of approximately 11 mV/m at an altitude of 101 km. As the altitude increases, E_z decreases to zero at 115 km, then becomes slightly negative, and then increases back to zero at 121 km. This curve suggests that E_h is almost negligible at 130 km near the peak of the Pedersen current. Therefore, the upper current layer near 130 km is almost entirely Pedersen current. In addition, the large peak in the curve at 101 km suggests that the lower current layer that peaks in the vicinity of a 105-km altitude consists primarily of Hall current. This curve also indicates that very little, if any, current flows between the lower and upper current layers in the absence of attraction that leads to overlap.

26
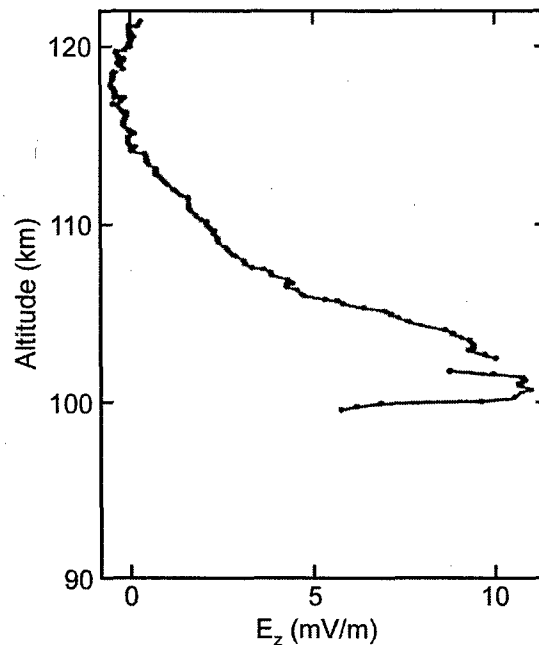
*Figure 3-6. Noontime Altitude Profile of Vertical Polarization
Field E_z Measured at Thumba, India, as Reported by Sartiel (Reference 13)*
(Taken from Onwumechili (reference 4), p. 179)

3.3 CURRENT DISTRIBUTION OF THE EEJ

Ionospheric currents have been measured from sensors aboard rockets. Rockets determine the ionospheric current density through the measurement of its magnetic field gradient. These measurements do not include the ambient magnetic field whose primary component is the geo-magnetic field. Onwumechili (reference 4) lists 76 rocket measurements of ionospheric currents that were made between 1948 and 1973. Most of the earlier rocket measurements were made with proton precision magnetometers, while many of the later measurements were made with vapor magnetometers (rubidium plus cesium). Rocket measurements provide the most direct measurement of studying ionospheric currents because their measurements are made *in situ*. Unfortunately, each rocket flight is very costly and provides only a transitory sampling above a very limited space. Rocket measurements have contributed significantly to the present under-standing of the EEJ and other ionospheric current systems. Figure 3-2 shows the ionospheric current density as a function of altitude that was obtained from rocket measurements above Thumba, India.

In addition to rockets, ionospheric currents have been determined from magnetic field measurements made aboard satellites. Four satellites that have been used in the measurement of the EEJ are the

1. Polar Orbiting Geophysical Observatory (POGO) satellites,
2. Magnetic satellite (Magsat),
3. Ørsted satellite, and
4. CHAMP satellite.

The POGO system is characterized by a wide variation in altitude of 400–1100 km and a rapid transit of local time. From POGO data, one is able to extract observations within 2 hours of noon, which is the optimum local time for electrojet measurements. Unfortunately, the fast transit time of POGO results in a limited amount of data from each passage of the equator. Magsat crossed the equator only at dusk and dawn, when the ionospheric currents are rather weak. As a result, Magsat was used to study the geomagnetic variations due to ionospheric currents only at dusk and dawn. Ørsted has a much slower transit time than the other satellites, which allows it to take more data with each pass of the equator. Because Ørsted is at a high altitude range (640–865 km), the EEJ signature is very weak, and sophisticated signal processing techniques must be used to extract it (reference 14).

According to Luhr et al. (reference 15), the CHAMP satellite has a low orbit (altitude ≈ 430 km) and is equipped with high-precision magnetometers, resulting in the measurement of the spatial structure of the EEJ with unprecedented accuracy. To isolate the field produced by the EEJ, the fields generated by other sources (e.g., main geomagnetic field, ground currents, and lithospheric magnetization) are removed from the measured data. Rather than determining the EEJ current density through interpretation of the magnetic field data (as is normally performed) obtained from the CHAMP satellite, Luhr et al. (reference 15) applied an EEJ current model consisting of 81 east-west oriented line currents spaced apart by 0.5° in latitude and located at an altitude of 108 km, in the vicinity of the EEJ current density peak. The intensities of the 81 independent line currents were derived through linear inversion of the observed magnetic field residuals at the various satellite positions. First-order corrections were applied to the line current model in order to account for current closure at the morning and evening terminators. Luhr et al. interpreted the magnetic field variations observed by CHAMP in terms of ionospheric currents from which the EEJ characteristics were deduced.

28

As explained in section 3.2, the EEJ is an eastward-directed current located in the vicinity of the dip equator at a mean altitude of 106 km. Figure 3-2 shows an altitude profile obtained from rocket measurements of the EEJ at 11:08 AM LT above Thumba, India, located just below the dip equator. The current density plot shows a peak of approximately 9.4 A/km^2 at an altitude of about 105 km. The EEJ current monotonically decreases with altitude on both sides of this peak. Notice that the altitude thickness of the Cowling conductivity layer is nearly twice that of the EEJ current layer. As previously explained, a large Hall current drives the EEJ.

Figure 3-7 shows plots of the direct-current electric field, current density, and plasma density as a function of altitude of the EEJ obtained from rocket measurements made above Alcantara, Brazil, at 10:56 AM LT. These plots were obtained from Pfaff et al. (reference 16). The EEJ current density peaks at 8 A/km^2 at an altitude near 105 km. This altitude is slightly lower than that corresponding to the peaks of current density profiles observed off the coast of Peru and over India.
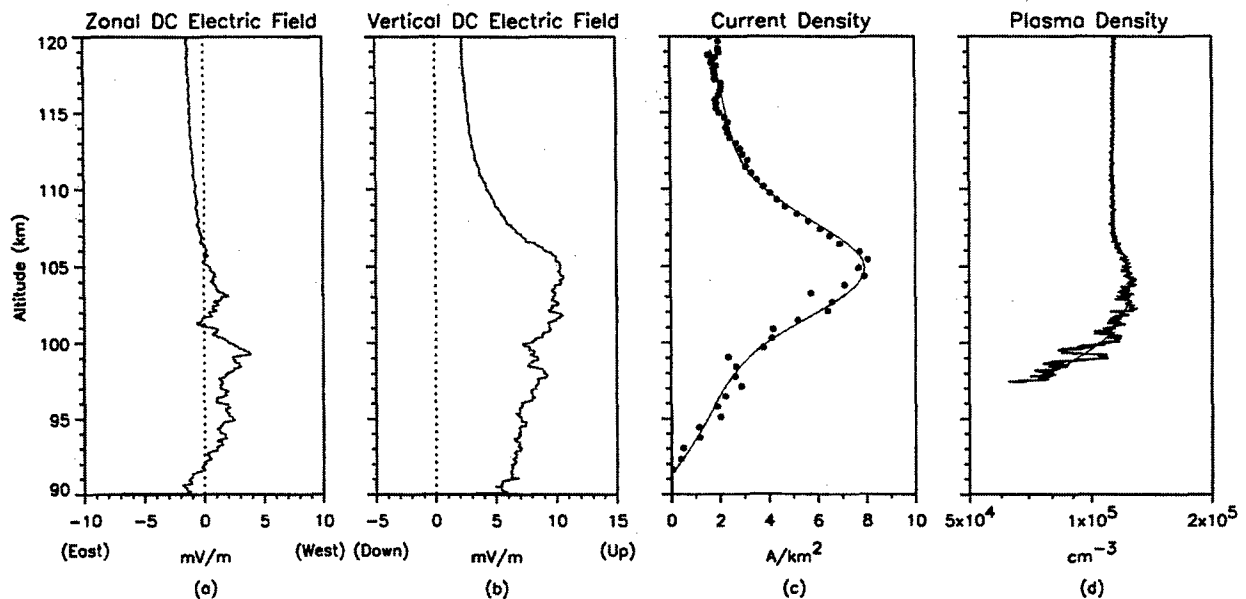
Note: Thin solid lines in (c) and (d) represent empirical fits to the data.

Figure 3-7. Plots of (a) East-West Electric Field, (b) Vertical Electric Field, (c) Current Density, and (d) Plasma Density as a Function of Altitude Obtained from Rocket Measurements Above Alcantara, Brazil
(Taken from Pfaff et al. (reference 16), p. 1669)

The EEJ is most intense over a time period that extends from 10:00 AM to 2:00 PM LT and reaches its maximum intensity between 11:00 AM and 12:00 PM LT (reference 4). Outside of this time period, the EEJ decreases significantly and usually diminishes at nighttime. This observation is compatible with altitude plots of the conductivity components, which show a significant decrease in their midnight profiles when compared with their noontime plots. As a result, measurements of the EEJ are typically performed during the period of maximum intensity. In general, measurements have indicated that outside of the auroral and polar regions, ionospheric currents do not normally flow in the nighttime in the dynamo region (90–150 km) in which Sq currents flow. Consequently, the geomagnetic field measured at nighttime is used as the datum or reference for determining the Sq field components ΔX, ΔY, ΔZ produced during the daytime (reference 4).

The magnetic fields produced by earth-induced currents must be accounted for when measurements are made of the ionospheric currents. Rishbeth and Garriott (reference 6) indicate that the currents induced in the earth from the overhead ionospheric currents contribute approximately one-third to the observed diurnal geomagnetic field variation. Forbush and Casaverde (reference 17) represented the internal magnetic field produced by currents induced in the earth from the overhead EEJ by an image electrojet current source of the same width as the EEJ and flowing westward at a depth of 600 km in the earth. In their model, the earth is assumed to be planar (in the neighborhood of interest) and is represented by two layers, i.e., a top nonconducting layer of thickness 250 km and perfectly conducting at depths greater than 250 km. An alternate approach to determine the earth-induced fields is via integral transform methods (reference 4).

As previously shown, the EEJ is an eastward-directed current layer located in the vicinity of the dip equator at a mean altitude of 106 km. The EEJ current density decreases with latitude away from the dip equator and vanishes at approximately $\pm 3°$ dip latitude (reference 4), which is referred to as the current focus. At latitudes beyond the current focus, the vertical electric field reverses to the downward direction, resulting in a reverse in the direction of the Hall current and a westward flow of the EEJ. The reversal in the vertical electric field is attributed to an increase in the local vertical field E_L associated with the local zonal winds with positive vertical shear. E_L is directed downward and reaches a maximum at about $\pm 5°$ dip latitude. In addition, the curvature of the magnetic field lines through the dynamo region results in minimizing the vertical Hall polarization field E_h at approximately $\pm 5°$ dip latitude.

30

Figure 3-8 shows altitude profiles of the ionospheric current density obtained from rocket measurements made off the coast of Peru at 4.5° dip latitude as reported by Maynard (reference 18). The plots reveal two current layers. The lower current layer flows in the westward direction and corresponds to the return current of the EEJ. The upper current layer flows eastward and is associated with the *WSq* system. Note that the upper layer current is more intense than the lower layer current. Similar altitude profiles were obtained from other rocket measurements for this dip latitude. Onwumechili (reference 4) notes that the westward-directed return current of the EEJ spreads very thinly (in latitude) over an area of more than four times the area of the forward current and is, therefore, difficult to detect (see figure 3-10).
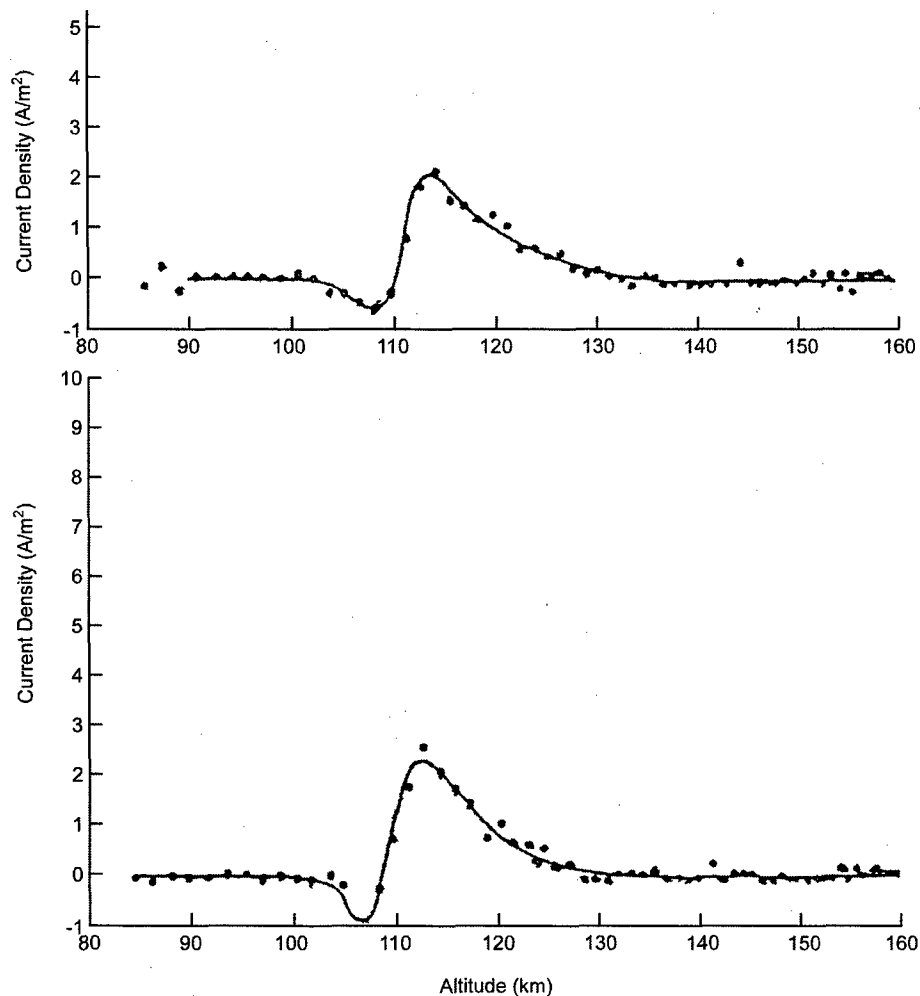
Note: Top curve refers to the rocket descent; bottom curve refers to the rocket ascent.

Figure 3-8. Altitude Profiles of Current Density off the Coast of Peru Above 4.5° Dip Latitude at 11:38 AM LT, as Reported by Maynard (Reference 18)
(Taken from Onwumechili (reference 4), p. 131)

Various empirical models of low-latitude ionospheric currents have been derived for fitting the data obtained from rocket and satellite measurements. Onwumechili (reference 4) has derived a continuous distribution of current density model that is two dimensional, with both a width and a thickness. Referring to the coordinate system shown in figure 3-1 with magnetic meridian (x,z) plane, the ionospheric current density J (A/m^2) at a point (x, z) is given by

$$J = u_y J_0 \left[\frac{a^2(a^2 + \alpha x^2)}{(a^2 + x^2)^2} \right] \left[\frac{b^2(b^2 + \beta z^2)}{(b^2 + z^2)^2} \right], \qquad (3\text{-}30)$$

where J_0 is the peak current density at $(x,z) = (0, 0)$, a and b are constant scale lengths along x and z, respectively, and α and β are dimensionless constants controlling the distribution of current along x and z, respectively. Note that the current decreases to zero with increasing vertical and latitudinal distances from the center at $(0, 0)$. The current density parameters J_0, a, α, b, and β are determined by fitting measured data to formula (3-30). Once these parameters have been determined, some of the characteristics of the current distribution, along with the magnetic field produced by it, can be calculated.

Sometimes it is more convenient to describe the ionospheric current in terms of an equivalent surface current distribution. This surface current is the height-integrated current density J_s (A/m) and is given by (reference 4)

$$J_s = u_y J_{so} \left[\frac{a^2(a^2 + \alpha x^2)}{(a^2 + x^2)^2} \right], \qquad (3\text{-}31)$$

where

$$J_{so} = bJ_0 \left[\frac{(1 - \beta)bL_2}{(b^2 + L_2^2)} + (1 + \beta) \tan^{-1}\!\left(\frac{L_2}{b}\right) \right]. \qquad (3\text{-}32)$$

In these expressions, J_{so} is the peak intensity on the current axis $x = 0$ and L_2 is half of the altitude extent of the current layer. Onwumechili obtained the above formulas through integration of the current distribution (3-30) over the height variable z.

Because β is usually positive, Onwumechili defines the half-thickness p at half of the peak density as

$$p = b \sqrt{(\beta - 1) + \sqrt{1 + (\beta - 1)^2}} .$$ (3-33)

Half of the latitudinal width or the focal distance w of the current is given in kilometers or degrees as

$$w^2 = -\frac{a^2}{\alpha} .$$ (3-34)

When $\alpha < 0$, the current density has two equal minimal values J_{sm} at distances x_m on the sides of the current axis given by

$$\frac{J_{sm}}{J_{so}} = \frac{\alpha^2}{4(\alpha - 1)} ,$$ (3-35a)

$$x_m^2 = \frac{a^2(\alpha - 2)}{\alpha} .$$ (3-35b)

The total ionospheric current I corresponding to expression (3-30) is

$$I = aJ_{so} \left[\frac{(1 - \alpha)aL_1}{(a^2 + L_1^2)} + (1 + \alpha) \tan^{-1}\left(\frac{L_1}{a}\right) \right] ,$$ (3-36)

where L_1 is the latitudinal extent of the current from its axis to where it terminates. An equation for determining L_1 is obtained by setting $I = 0$ in the above formula, resulting in

$$\left(\frac{L_1}{a} + \frac{a}{L_1}\right) \tan^{-1}\left(\frac{L_1}{a}\right) = \frac{(\alpha - 1)}{(\alpha + 1)} ,$$ (3-37)

where $\alpha < -1$. The total forward current I_F flowing eastward between the two current foci ($|x| < w$) is given by

$$I_F = aJ_{so} \left[\sqrt{-\alpha} + (1 + \alpha) \tan^{-1}\left(\frac{1}{\sqrt{-\alpha}}\right) \right] .$$ (3-38)

The current distribution along the latitudinal or x-direction is controlled by the parameter α. For $\alpha \geq 0$, the current flow is entirely along the eastward or y-direction. For $\alpha < 0$, the current flow between the foci ($|x| < w$) is along the eastward direction and then reverses direction to flow westward along the sides. Figure 3-9 compares the current distributions for $\alpha = 0$ and $\alpha = -2$. For $0 \leq \alpha \leq 2$, there is only one maximum J_{so} at $x = 0$, and there are no minima, as shown in figure 3-9(c). For $-\alpha > 2(1+\sqrt{2})$, the minima J_{sm} become larger in magnitude than the maximum J_{so}. For $\alpha > 2$, the peak value J_{so} at $x = 0$ becomes a minimum and the maximum current is at $x = \pm x_m$ as given in expression (3-35b).

Onwumechili (reference 4) has fit his formula for continuous distribution of current density (3-30) to the rocket-observed altitude profiles of current density of the lower layer EEJ and the upper layer WSq current system. Onwumechili determined that it is desirable to fit the lower part of the altitude profile below the peak current density separately from the upper part because the profile is not symmetrical about the altitude of the peak density. From measured data at well-spaced points along the altitude profile, the parameters of the model may be determined by the method of least squares.

Table 3-2 compares the current density model fitting parameters of the EEJ for the rocket profiles observed above Thumba in Southern India and those observed off the coast of Peru in South America. The fitting parameters over each site are based on eight rocket measurements, with the mean, standard deviation, and median listed. Note in table 3-2 that C_0 is the peak current density in formula (3-30) on the current axis at $(x,0)$ of the EEJ above the location (x,h) of rocket launch. Because the measured EEJ current density profiles are not symmetrical about the altitude of the peak current density, the lower and upper parts of the profiles are fitted separately. Consequently, in table 3-2, the subscripts 1 and 2 refer to the part of the profile below and above the peak current density, respectively, and the subscript 3 refers to the average of top and bottom parts of the profile.
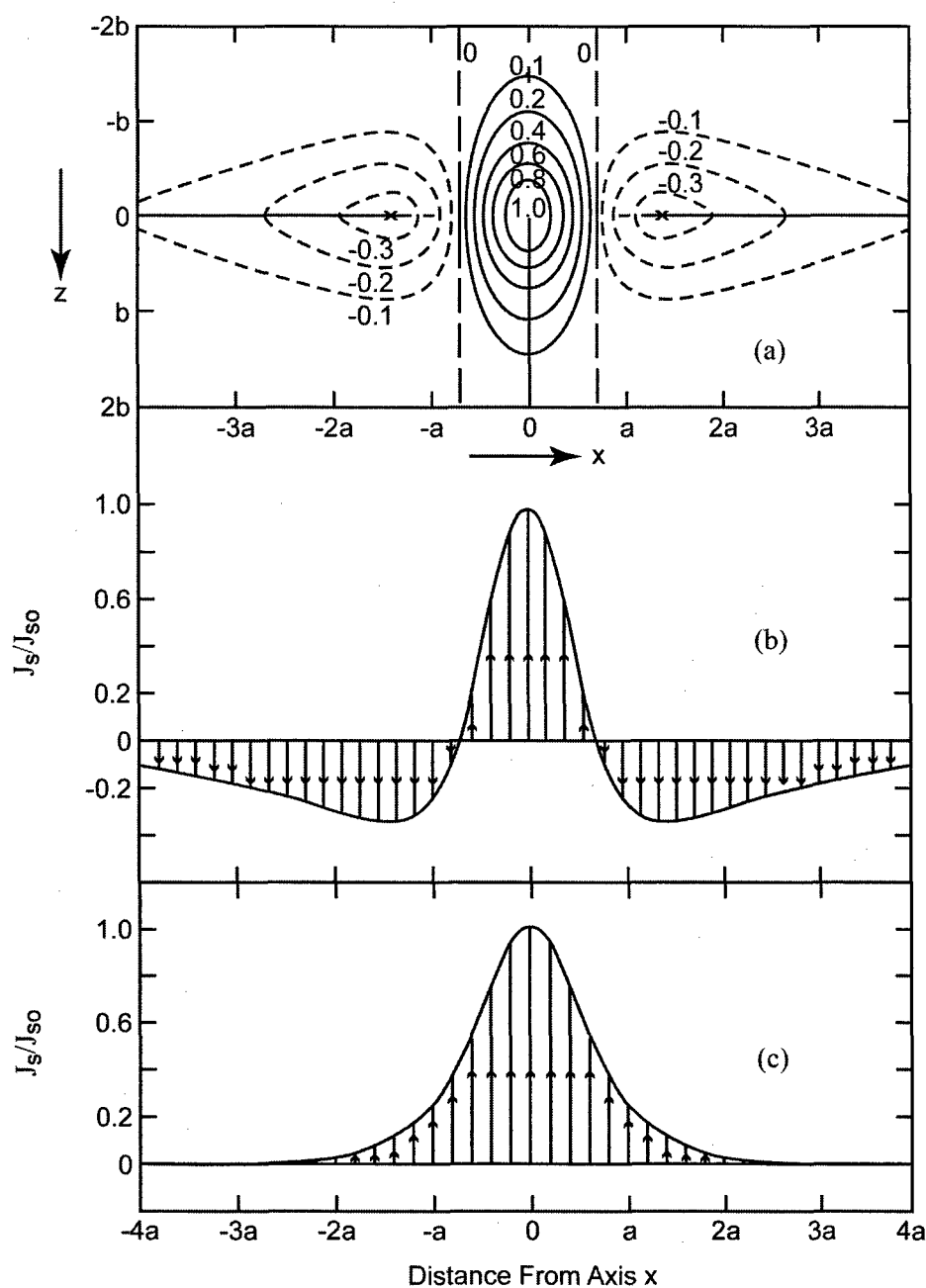
Note: In plot (a), eastward current plotted in solid contours; westward current plotted in broken contours.

Figure 3-9. *(a) Contours of EEJ Current Density J Relative to Its Peak Current Density J_O at the Center as Computed from Formula (3-30) with $\alpha = -2$ and $\beta = 0$; and Variation of EEJ Height-Integrated Current Density J_s Relative to its Peak Intensity J_{so} as Computed from Formula (3-32) with (b) $\alpha = -2$ and (c) $\alpha = 0$*

(Taken from Onwumechili (reference 4), p. 147)

Table 3-2. Comparison of the Parameters Fitting the Altitude Profiles of the EEJ Current Density Measured by Rockets Above Southern India and off the Coast of Peru

(Taken from Onwumechili (reference 4), p. 151)

Parameter	INDIA				PERU			
	Count	Mean	Std. Dev.	Median	Count	Mean	Std. Dev.	Median
$C_0(A/km^2)$	8	8.73	3.40	9.01	8	9.71	2.65	9.88
$J_0(A/km^2)$	8	9.42	3.62	9.82	8	10.47	2.26	10.77
$J_s(A/km)$	8	130	53	130	8	130	34	138
$J_{s0}(A/km)$	8	139	57	140	8	141	32	141
$p_1(km)$	8	5.34	0.78	5.24	8	5.26	0.69	5.13
$p_2(km)$	8	6.34	1.30	6.33	8	5.65	0.82	5.36
$p_3(km)$	8	5.81	0.76	5.92	8	5.47	0.49	5.51
$b_1(km)$	8	7.2095	1.6115	6.7865	8	8.1606	1.8762	7.9430
$b_2(km)$	8	8.3016	2.0476	8.6637	8	7.5798	1.9489	7.3095
$b_3(km)$	8	7.8434	1.8382	8.1130	8	7.9754	1.5119	7.7105
β_1	8	0.3687	0.3406	0.2815	8	0.0240	0.3275	0.0460
β_2	8	0.4306	0.3699	0.4975	8	0.3905	0.3921	0.4940
β_3	8	0.3892	0.2933	0.3341	8	0.1773	0.3417	0.3095

Note: Subscripts 1 and 2 refer to the part of the profile below and above the altitude of the peak current density, respectively; subscript 3 refers to the whole profile.

This table suggests that there is no significant difference between the current densities and intensities of the EEJ observed over India and Peru. This observation is in agreement with the results obtained from satellite data. From this table, the following observations are made:

1. The half thicknesses p_1, p_2, and p_3 are smaller above Peru than over India.

2. The parameter b is about the same over India and Peru.

3. The current distribution parameters β_1, β_2, and β_3 are smaller at Peru than at India.
4. The current density is larger over Peru.

5. The width of the EEJ is larger above India.

Therefore, these results indicate that the EEJ current above Peru is greater in intensity but narrower in width than that over India.

Figure 3-10 is a plot of the longitude average of the height-integrated current density J_s of the EEJ as a function of magnetic dip latitude as obtained from POGO satellite data. The curve was generated by fitting Onwumechili's height-integrated current density model given in formulas (3-31) and (3-32) to the measured data. The plot shows that the EEJ current is a

maximum (162 A/km) at the dip equator ($x = 0$) and decreases to zero at the focal latitudes $x = \pm w = \pm 2.76°$. The EEJ flows eastward over the region $|x| < w$. The reverse westward return current increases from zero at $x = \pm w$ to a peak of $J_{sm} = -37.3$ A/km^{-1} at the latitudes $x_m = \pm 5.18°$. For $|x| > x_m$, the return current decreases with dip latitude to zero. Note that from expression (3-36), all of the forward current has returned by latitude $L_1 = 11.75°$. Onwumechili (reference 4) notes that when the distances w, x_m, and L_1 are reduced, the current distribution contracts and the current intensities J_{so} and J_{sm} increase in magnitude.
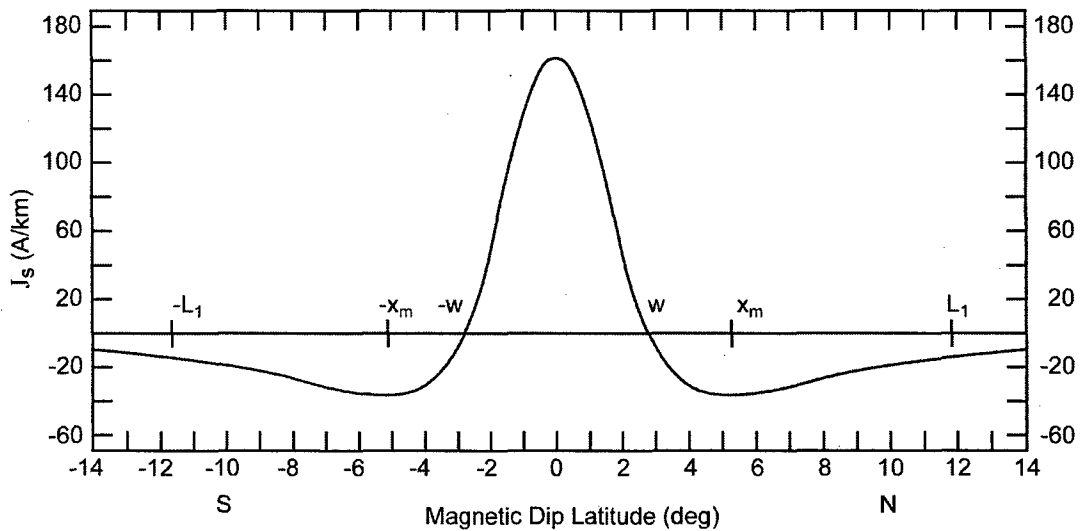
(Note that focal latitude $w = 2.76°$; peak return height-integrated current density $J_{sm} = -37.3$ A/km and occurs at $x_m = 5.18°$ dip latitude; and latitudinal extent of the current $L_1 = 11.75°$ dip latitude.)

Figure 3-10. Latitudinal Profile of EEJ Height-Integrated Current Density J_s Derived from the POGO Satellites Daytime Mean Values of
$J_{so} = 162 \pm 45$ A/km, $a = 3.42 \pm 0.06°$, and $\alpha = -1.533 \pm 0.05$
(Taken from Onwumechili (reference 4), p. 193)

Recent results reported by Luhr et al. (reference 15) that are based on CHAMP satellite observations of the noontime EEJ indicate that the average peak of the height-integrated current density J_{so} is approximately 150 A/km^2, which is fairly close to the mean values listed in table 3-2, but less than the 200 A/km^2 value reported by Jadhav et al. (reference 19). Luhr et al. also observed that the peaks of the EEJ return current are located at an average of $\pm 5°$ dip latitude and are fairly independent of longitude. In addition, they also found that the total EEJ eastward current has an average value of 65 kA and is about three times as strong as the westward return current. Luhr et al. determined that the noontime EEJ appears to be strongest at a longitude of

60° W (Central South America) and weakest at 40° E (Eastern Africa). The maximum location at 60° W is compatible with previous measurements, while the minimum at 40°E was also observed from Ørsted satellite measurements, but not from POGO or Magsat satellite measurements. Luhr et al. observed that the EEJ width varies only ±10° over all longitudes, with larger widths found over Indonesia (120° E) and the Eastern Pacific (120° W) and narrower widths above Africa. These observations differ somewhat from those made by Onwumechili (reference 4) and Jadhav et al. (reference 19).

Onwumechili (reference 4) has derived expressions for the magnetic fields produced by the ionospheric current densities J and J_s given in formulas (3-30) and (3-31), respectively. Jadhav et al. (reference 19) have applied this model to magnetic field data obtained from the Ørsted satellite to determine the longitudinal structure of the EEJ, as well as the sources responsible for its diurnal variation.

3.4 MAGNETIC FIELD OF THE EEJ

The magnetic field of the EEJ has been measured by magnetometers located on rockets, satellites, and the ground. (Rocket and satellite measurements were discussed in section 3.3.) Ground-based magnetometers operate somewhat differently from those on satellites, but their output, which consists of three mutually perpendicular components of the perturbation in the magnetic field from its steady value, is the same. These magnetic field perturbations are usually expressed in terms of the components (X, Y, Z) or (H, D, Z), as defined in figure 2-2, and are sometimes expressed in terms of the geomagnetic coordinate system as described in figure 2-4. It is impossible to derive the true horizontal ionospheric current distribution uniquely from ground magnetometer measurements because they are a superposition of contributions from many sources in addition to the EEJ. As a result, equivalent current distributions have been derived.

The plots of the altitude variation of the ionospheric current density in figures 3-2 and 3-8 showed the existence of two Sq current layers. The lower layer is the EEJ and the upper layer is associated with the worldwide part of the Sq commonly referred to as the WSq current system. Each of these currents produces a magnetic field. Because the EEJ is an eastward current, it does not produce an eastward component of magnetic field (ΔY) very close to its axis. However, near

the focus of the EEJ at approximately 3°N dip latitude, ΔY produced by the EEJ is a maximum. The EEJ has a noticeable effect on the quiet daily variation of the north component of the geomagnetic field $Sq(X)$, and, therefore, on the quiet daily variation of the horizontal geomagnetic component $Sq(H)$.

Figure 3-11 shows plots of the $Sq(X)$ and $Sq(Z)$ fields as a function of dip latitude that were measured across the dip equator in Brazil at 11:30 AM LT. These fields include contributions from the EEJ and the WSq currents. For both field components, the dashed curve refers to the WSq field and the solid curve refers to the combined field from both currents. The plot of the north field component $Sq(X)$ shows that the EEJ greatly enhances the field in the region surrounding the dip equator. The portion of the combined field curve that drops below the $WSq(X)$ curve is caused by the return currents of the EEJ. At greater distances from the dip equator, the EEJ field is negligible, which results in an overlap of the curves. Onwumechili (reference 4) has demonstrated that the widths of the EEJ and its corresponding horizontal magnetic field ΔH decrease as the EEJ intensity increases.

The plots of the vertical field component $Sq(Z)$ in figure 3-11 indicate that the fields produced by the EEJ and WSq currents have similar asymmetrical profiles across the dip equator. The EEJ increases the amplitude of $Sq(Z)$ to more than double that of $WSq(Z)$ and tends to center it on the dip equator. At the edge of the EEJ where the $Sq(Z)$ from the EEJ is a maximum, it completely dominates the $WSq(Z)$ field. The $Sq(Z)$ component is sensitive to the north-south movement of the EEJ. However, because of the presence of the WSq current, the $Sq(D)$ component is more reliable for detecting the north-south movement of the EEJ.
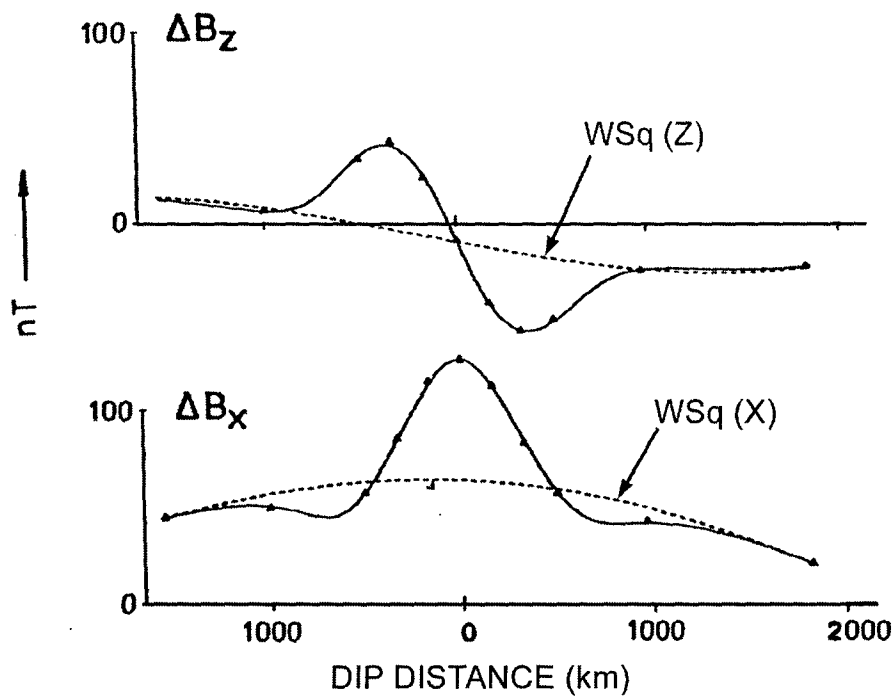
***Figure 3-11. Latitudinal Profiles of the Daily Ranges of Northward Magnetic Field ΔB_x and
Vertical Magnetic Field ΔB_z Across the Dip Equator in Brazil,
Measured on 14 November 1971 at 11:30 AM LT***
(Taken from Onwumechili (reference 4), p. 261)

To describe the seasonal variations of the ionospheric current systems, the months of the year are grouped as follows:

D months: January, February, November, and December;

E months: March, April, September, and October;

J months: May, June, July, and August.

The EEJ is normally more intense in the equinoxes (E season) than in the solstices (D and J seasons). Consequently, the magnetic field of the EEJ will also be larger in the equinoxes.

4. ALTITUDE STRUCTURES OF IONOSPHERIC CURRENT LAYERS

Numerous experiments have provided strong evidence for the existence of a double current layer system at the dip equator, where the lower current layer is the EEJ. Onwumechili (reference 4) has identified the upper ionospheric current layer with the worldwide part of the *Sq* current system (often referred to as *WSq* currents). This upper current layer generally flows eastward from the dip equator to the *Sq* current focus (point of zero current), but flows westward from the *Sq* current focus and the high latitudes. The median altitude of the upper current layer is approximately 123 km, with a median altitude extent of 18 km.

Figure 4-1 is a contour plot of the *WSq* current distribution as a function of latitude and local time that was obtained by Onwumechili by fitting the magnetic field functions derived from the continuous distribution of current density model (3-30) to the observed geomagnetic *Sq* variations. The contours in this figure are streamlines of the *WSq* current. The number associated with each contour indicates the total counterclockwise current (in kA) flowing between the line and the boundary between the two current vortices. The current is more intense in regions where the contours are more crowded. The "+" marks in figure 4-1 refer to the *WSq* current foci (i.e., points of zero current). The plot shows that the *WSq* currents exist over a period extending from 6:00 AM to 6:00 PM LT. The currents are most intense at noontime with a focus at a dip latitude of approximately 35°.

Table 4-1 is a summary of the daytime altitude structures of ionospheric current layers that are grouped into five regions or groups (Group 1 through Group 5) according to dip latitude. This table was derived by Onwumechili (reference 4) and is based on data obtained from rocket measurements. Note that the lower current layer has been observed in the first four regions. Based on the data currently available, the lower current layer extends from the equator to at least 20° dip latitude, but not beyond the *Sq* focus at about 35° dip latitude. The lower current layer flows eastward in regions 1, 2, and 4, but flows westward in region 3 ($4° < I < 7°$), corresponding to the return current of the EEJ. The upper current layer flows eastward in regions 1–4 ($0° < I < 35°$) and westward in region 5 ($35° < I < 70°$). However, the direction of the upper current layer is erratic in the polar cap region. Note that the single current layer system listed as group 1(x) in table 4-1 occurs within 0° and 0.5° latitude and is a hybrid between the lower and upper layers.
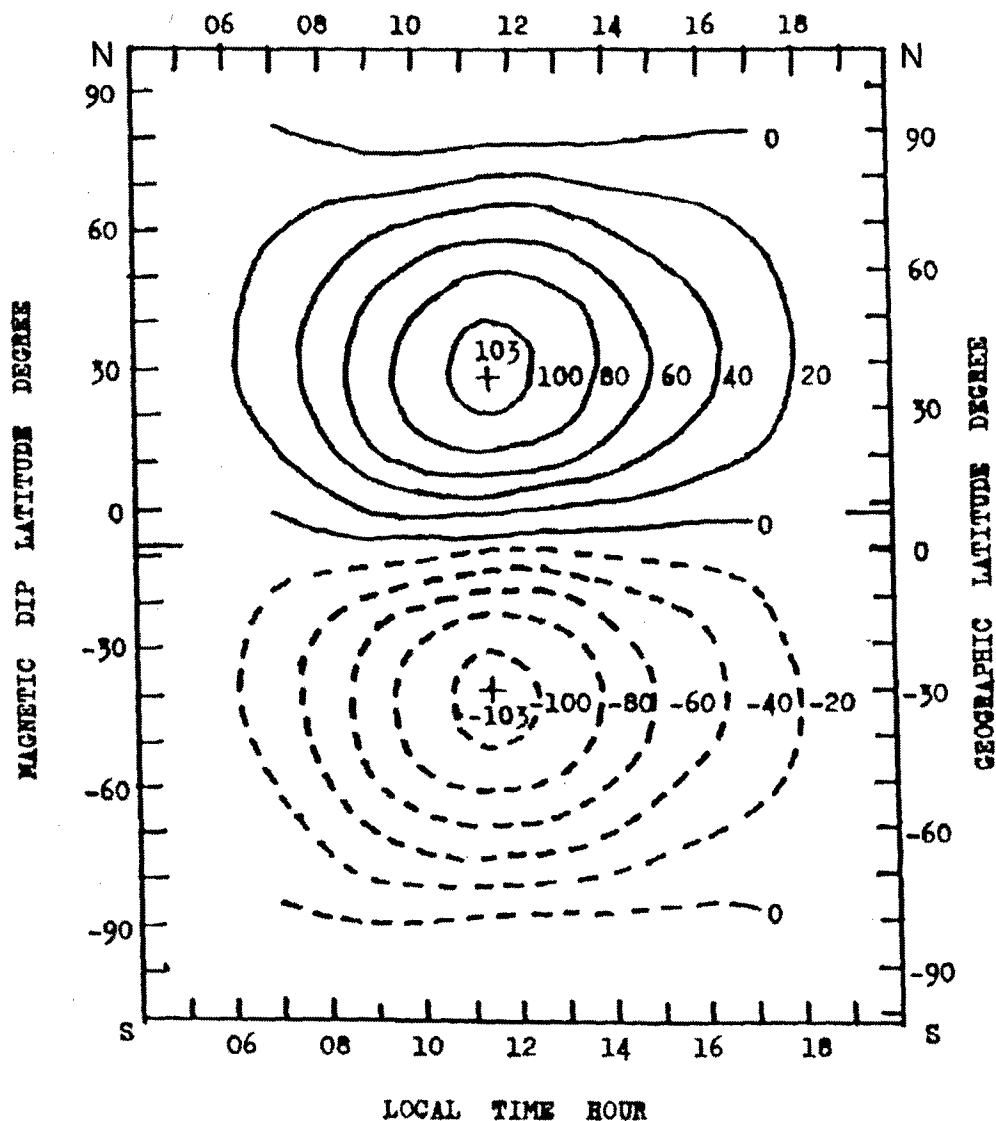
Note: Continuous lines indicate counterclockwise current and broken lines indicate clockwise current; 20,000-A flow between two consecutive contour lines. The longer bar on each vertical axis is the zero level on the opposite axis.
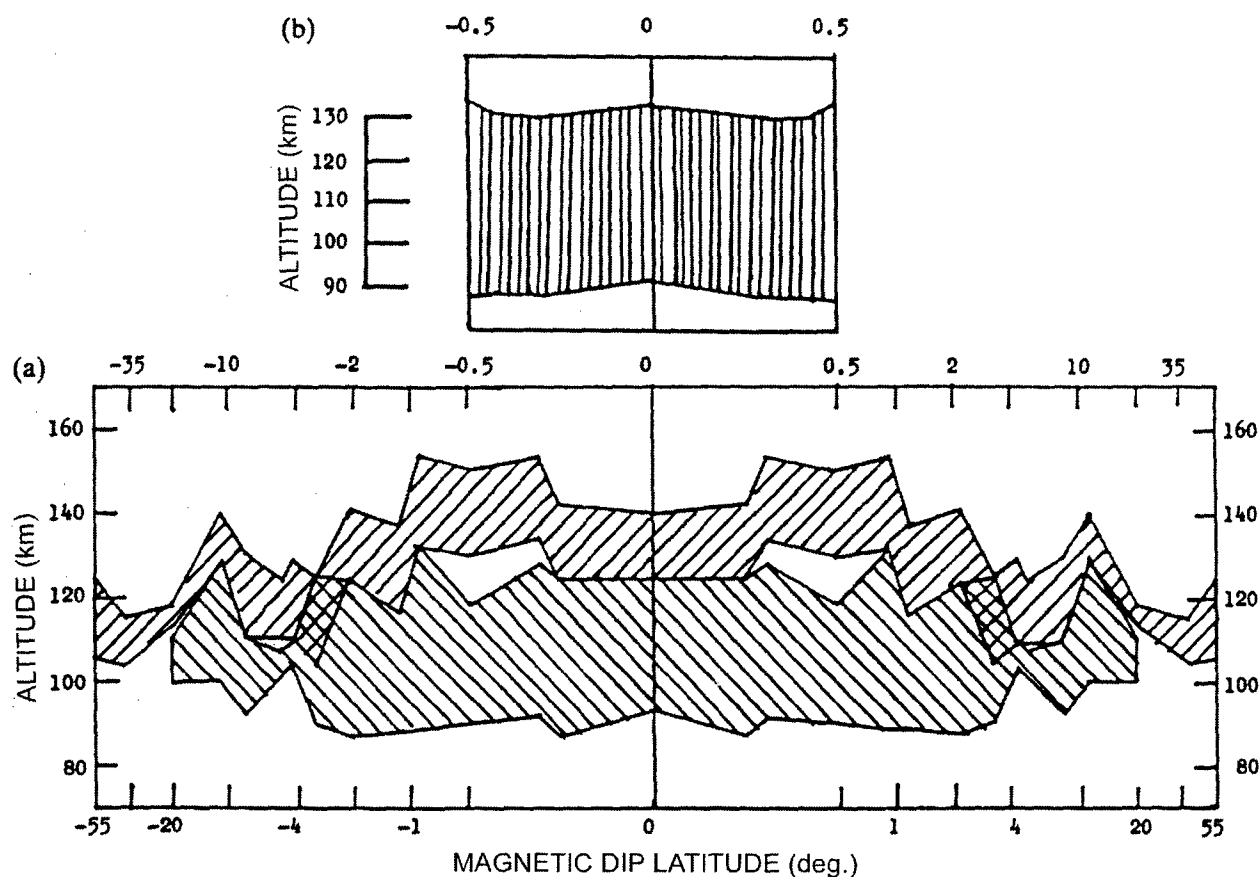
Figure 4-1. Subsolar Elevation of WSq Current System Derived from Indian Observatories Data of 1986
(Taken from Onwumechili (reference 4), p. 175)

Table 4-1. Global Comparison of the Altitude Structures of Ionospheric Current Layers
(Taken from Onwumechili (reference 4), p. 138)

	System Field Change ΔB_0 nT	Layer 1 current Direction	Layer 1 Peak Current Density A km⁻²	Layer 1 Peak current Density Altitude km	System Lower Edge Altitude km	Layer 1 Upper Edge Altitude km	Layer 1 Altitude Extent km	Layer 2 Current Direction	Layer 2 Peak Current Density A km⁻²	Layer 2 Peak Current Density Altitude km	Layer 2 Lower Edge Altitude km	System Upper Edge Altitude km	Layer 2 Altitude Extent km	System Altitude Extent km
Group 1: Daytime within 0° to 2° dip latitude, with two layers														
Mean 162	E	8	106.7	90	122	32	E	1.1	136	128	147	19	57
Std. Dev. 98		3	1.5	3	6	8		0.8	8	10	8	5	9
Median 138		8	105.5	90	119	28		0.7	140	130	150	18	58
Group 2: Daytime within 2° to 4° dip latitude														
Mean 72	E		105.5	91.5	125	33.5	E		111.9	104	125	21	
Std. Dev. 24			1.2	2.3	5	5.5			0.7	5	4	8	
Median 80			106	91	125	33			111	100	125	25	
Group 3: Daytime within 4° to 7° dip latitude														
Mean	W	−3	106.3	103	108.3	5	E	2.4	113.7	108.7	127	18	24
Std. Dev.		4	0.6	1	0.6	1		0.4	0.6	0.6	2	3	2
Median 27		−0.9	106	103	108	6		2.4	114	109	129	20	24
Group 4: Daytime within 7° to 35° dip latitude, before the Sq focus														
Mean 30	E	1.6	105	96	115	19	E	1.0	123	115	130	15	34
Std. Dev. 20		0.3	8	5	9	7		0.8	8	9	9	8	11
Median 38		1.6	100	92	111	18		1.0	120	112	130	21	38
Group 5: Daytime with 35° to 70° dip latitude, between Sq focus and high latitudes														
Mean 16							W	J, −30	112	105	122	17	17
Std. Dev. 6								8	3	0.7	4	3	3
Median 15								J, −26	112	105	123	18	18
Group 1(x): Daytime within 0° to 2° dip latitude, hybrid system														
Mean 144	E	9	107	89							136		47
Std. Dev. 42		3	2	4							4		5
Median 120		9	106	90							135		46

Figure 4-2 illustrates the altitude extents of the upper and lower ionospheric current layers as a function of dip latitude. This illustration complements table 4-1 and clearly brings out the features of the ionospheric current systems. Onwumechili (reference 4) found that double-layer ionospheric currents were observed in approximately 60% of all rocket observations reported within the 0°–2° dip latitude region (group 1(x)). This is much lower than the expected percentage and is attributed to the reluctance of investigators to report a second layer in light of their interests in other experimental objectives. There are no significant differences in the altitude extent of the lower current layer with or without the presence of an upper layer. The altitudes of the lower edge and peak of the lower current layer are generally about the same regardless of the presence of an upper current layer. However, the upper edge of the lower current layer in a single-layer system is about 12 km in altitude above its altitude in a two-layer system. Figure 4-2 shows that there is often overlap between the two current layers. Unlike the lower current layer, the altitude of the peak current density of the upper layer varies considerably, i.e., from 125–152 km.

(b)

ALTITUDE (km)
130
120
110
100
90

-0.5   0   0.5

(a)

-35   -10   -2   -0.5   0   0.5   2   10   35

ALTITUDE (km)
160
140
120
100
80

-55   -20   -4   -1   0   1   4   20   55

MAGNETIC DIP LATITUDE (deg.)

Note: In the cross-hatched area of the transition zone, the lower layer is observed sometimes and the upper layer is observed in the same place at other times.

Figure 4-2. Latitudinal Profiles of the Altitude of Ionospheric Current Systems Observed by Rockets: (a) Basic Two-Layered Current Systems; (b) Hybrid Current Systems Observed Some of the Time within 0–0.5° Dip Latitude
(Taken from Onwumechili (reference 4), p. 142)

Altitude profiles of the ionospheric current density based on rocket measurements taken off the coast of Peru are shown for dip latitudes of 0° and 8° in figures 4-3 and 4-4, respectively. Both plots clearly show the existence of two current layers. Figure 4-3 shows some overlap between the two current layers, with the lower layer much more intense than the upper layer. Figure 4-4 shows that the upper layer has a greater intensity than the lower layer.

Figure 4-3. Altitude Profiles of Current Density over the Pacific Ocean off the Coast of Peru Above 0° Dip Latitude at 11:16 AM LT, as Reported by Shuman (Reference 20)
(Taken from Onwumechili (reference 4), p. 118)

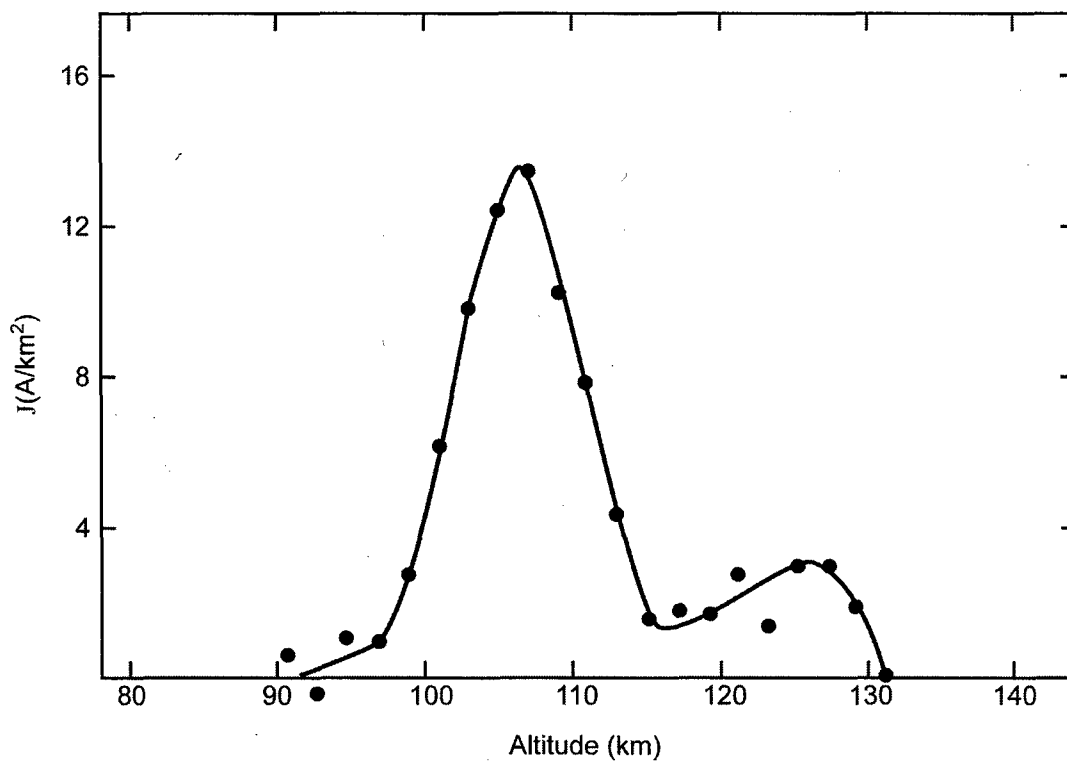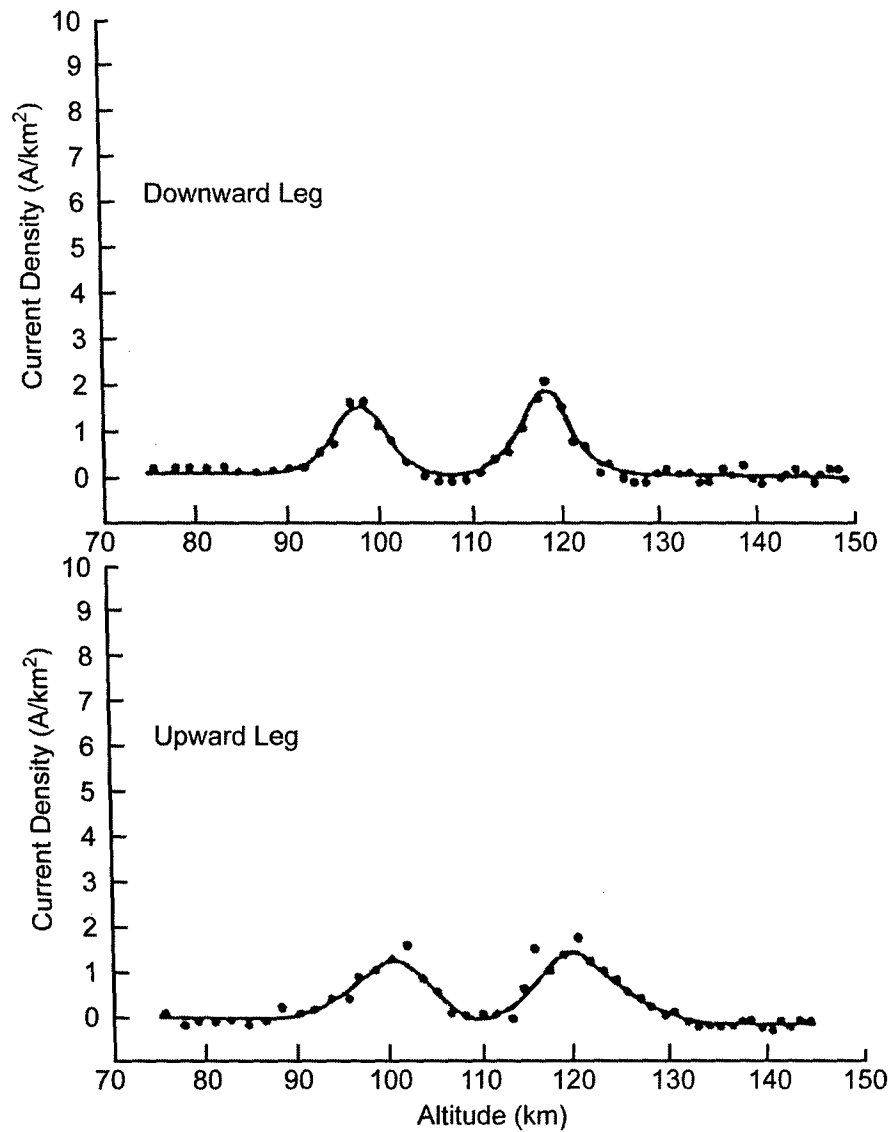Note: Top curve refers to the rocket descent; bottom curve refers to the rocket ascent.

Figure 4-4. Altitude Profiles of Current Density off the Coast of Peru Above 8° Dip Latitude at 12:14 PM LT, as Reported by Maynard (Reference 18)
(Taken from Onwumechili (reference 4), p. 116)

5. AURORAL ELECTROJET

The auroral electrojet (AEJ) is an intense horizontal electric current that flows in the D- and E-regions of the ionosphere at high latitudes (50–90 km and 90–150 km, respectively) in the auroral oval. In general, the AEJ current flows eastward in the afternoon and evening periods and flows westward in the morning, but its configuration is quite dynamic. Figure 5-1 is a simplified sketch of the AEJ current system. Without magnetic substorm activity, the demarcation line between the eastward and westward currents is located near midnight. The westward AEJ can also appear in the late evening hours prior to midnight when magnetic substorms are in their expansion stage. According to Kamide (reference 21), the westward AEJ is the most dominant feature of polar magnetic substorms, which start most often around local midnight and are accompanied by auroral substorms. During magnetically disturbed periods, the AEJ can extend into lower latitudes. The AEJ is much more variable than the EEJ because of the frequent occurrence of magnetic substorms at high latitudes.

Figure 5-1. Simplified Sketch of the Auroral Electrojet Current System
(Taken from Knecht (reference 5), p. 77)

Figure 5-1 shows an inflow of current into the morning half of the auroral oval and an outflow of current from the afternoon and evening half o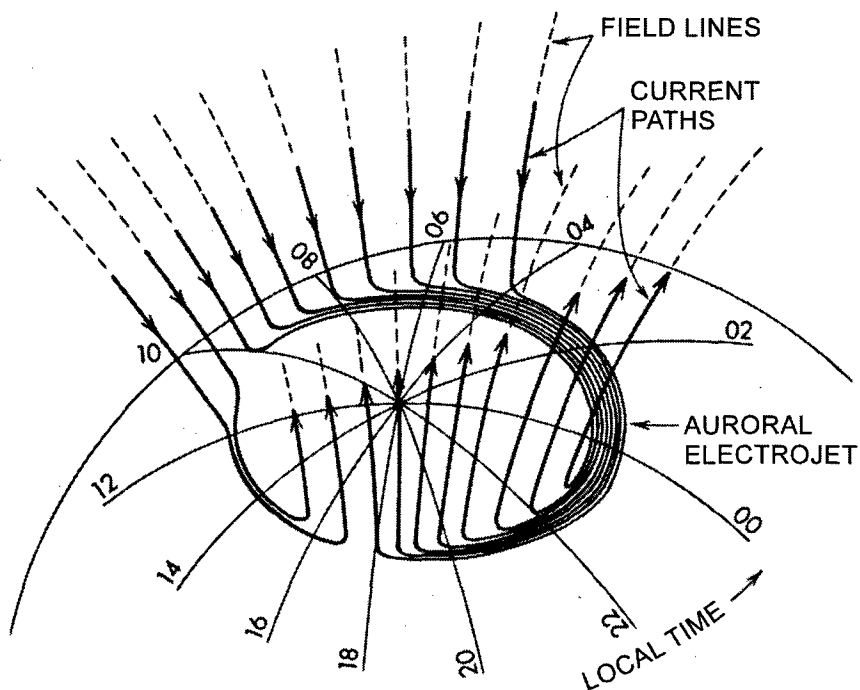f the auroral oval. These inflow and outflow currents, which travel along magnetic field lines, are referred to as the field-aligned current (FAC) system. FAC flows along magnetic field lines from one hemisphere to the other via the magnetosphere. The FAC is connected through the westward electrojet that flows along the nightside auroral oval. It is believed that the FAC is responsible for driving the AEJ. The FAC is more intense in the auroral region than in the dip equator region. The AEJ that appears in the auroral oval in the southern hemisphere is sometimes referred to as the austral electrojet.

The auroral ovals are bands that encircle the north and south geomagnetic poles where energetic particle precipitation takes place. The oval is closest to the geomagnetic pole on the day side and farthest away from it on the night side of the earth. Under quiet conditions, the oval extends between 68° and 78° geomagnetic latitude (reference 6). Figure 5-2 shows the location of the auroral oval in the northern hemisphere under moderate auroral activity. According to Knecht (reference 5), the oval approaches to within 2° of the geographic pole and dips as far south as 54° geographic latitude. Magnetic storms are associated with solar activity. During a magnetic disturbance, the auroral ovals expand in area and the auroral zone extends to lower latitudes. The enhanced ionization along the auroral oval that occurs as the result of a magnetic substorm determines the configuration of the AEJ.

The earth's magnetic field is frequently disturbed and undergoes variation other than the quiet Sq and L variations. If the geomagnetic field is severely disturbed, a magnetic storm is said to occur. The disturbance magnetic field associated with ionospheric currents principally flowing in the polar regions is referred to as DP (references 6 and 21). DP consists of two parts,

$$DP = DP1 + DP2. \qquad (5-1)$$

$DP1$ produces magnetic "bays" on magnetograms, i.e., abrupt magnetic disturbances lasting an hour or two, and is associated with intense auroral phenomena. The $DP1$ current system consists of an intense westward electrojet along the nighttime part of the auroral oval with return currents on either side. $DP2$ is a twin-vortex system with return currents that are not concentrated enough to be regarded as electrojets. The DP current systems are attributed to localized enhancements of the ionospheric conductivity and/or electric field (reference 6).

48
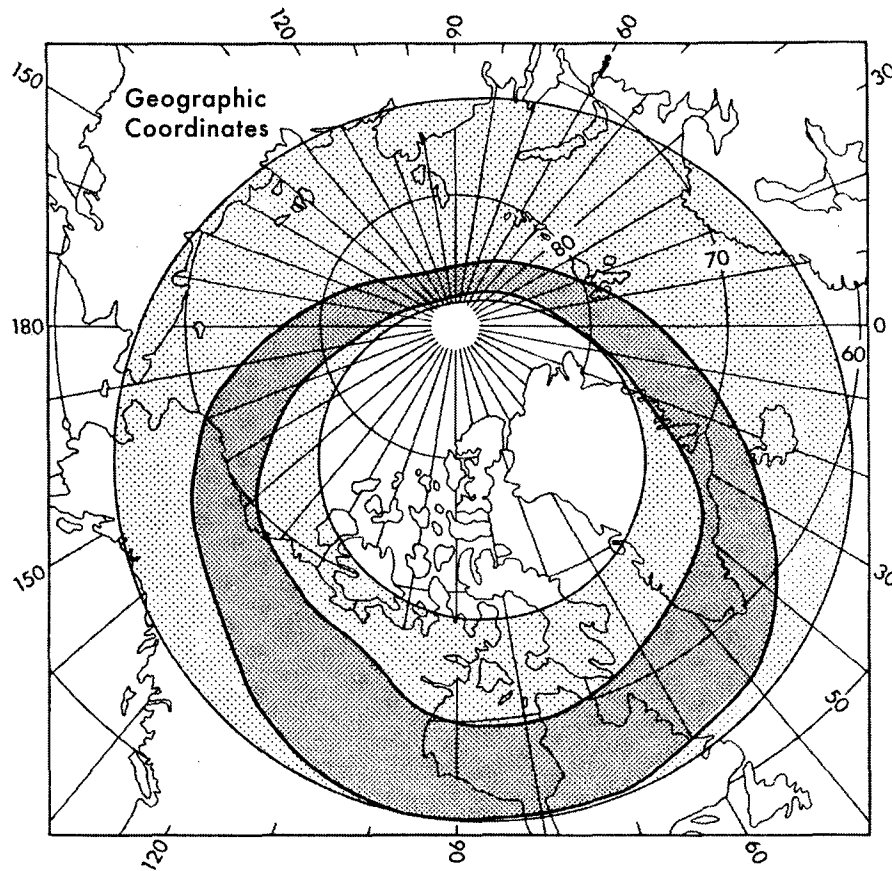
Note: Dark shading shows the oval at 0800 UT and the light shading indicates the area swept over by the oval during the day

Figure 5-2. Location of the Auroral Oval During Moderate Magnetic Storm Activity
(Taken from Knecht (reference 5), p. 74)

The ionospheric current density is given as the sum of the parallel, Pedersen, and Hall currents as expressed in formula (3-7). The primary direction of the AEJ current flow is perpendicular to the geomagnetic field B_0, resulting in the simplified expression

$$J_\perp = \sigma_p E_\perp + \sigma_h \, u_\| \times E_\perp , \qquad\qquad (5\text{-}2)$$

where $u_\|$ is a unit vector parallel to B_0 (see figure 3-1), $E_\perp$ is the component of E that is perpendicular to B_0, and σ_p and σ_h, the Pedersen and Hall conductivities, respectively, are given in expressions (3-10b) and (3-10c), respectively. The AEJ current is typically expressed in terms of a height-integrated current density J_s (references 21 and 22). If the above formula is

49

integrated with respect to altitude, one obtains the perpendicular component of height-integrated current density; i.e.,

$$J_{s\perp} = \int_{z_1}^{z_2} J_{\perp}\, dz = \Sigma_p E_{\perp} + \Sigma_h\, u_{\parallel} \times E_{\perp}\ ,$$

(5-3)

where Σ_p and Σ_h denote the height-integrated Pedersen and Hall conductivities, respectively. In expression (5-3), Brekke et al. (reference 22) took the limits of integration z_1 and z_2 as 90 km and 170 km, respectively. From formula (5-3), the height-integrated current density can be given in terms of geomagnetic north and east components, J_{sx} and J_{sy}, respectively, as

$$\begin{bmatrix} J_{sx} \\ J_{sy} \end{bmatrix} = \begin{bmatrix} \Sigma_p & -\Sigma_h \\ \Sigma_h & \Sigma_p \end{bmatrix} \begin{bmatrix} E_x \\ E_y \end{bmatrix},$$

(5-4)

where E_x and E_y refer to the geomagnetic north and east components, respectively, of the electric field.

To explain the existence of the AEJ, consider the illustration given in figure 5-3. Assume that a uniform westward electric field E_y exists in the highly conducting auroral zone of the ionosphere. Because the adjacent polar cap and subauroral regions are less conducting, positive and negative excess charges are accumulated at the poleward and equatorward boundaries, respectively, of the auroral zone. These excess charges will produce a southward polarization electric field E_x, resulting in a total electric field along the southwestward direction in the northern hemisphere. This polarization field produces secondary Pedersen and Hall currents. In the "classical" Cowling model of the AEJ (reference 21), the southward Pedersen current $\Sigma_p E_x$ due to the polarization electric field E_x completely cancels the northward Hall current $-\Sigma_h E_y$ associated with the primary westward field E_y, while the secondary Hall current $\Sigma_h E_x$ combines with the primary Pedersen current $\Sigma_p E_y$ to produce an intense westward electrojet J_{sy}.

50

x (North)

z ⊗ ──────► y (East)

(Vertical Down)

POLAR CAP REGION
(Less Conducting)

⊙ + ⊙ +

E_y

E_x

AURORAL REGION
(Highly Conducting)

◄────── $J_{sy} = \Sigma_p E_y + \Sigma_h E_x$

$J_{sx} = \Sigma_p E_x - \Sigma_h E_y$

⊗ − ⊗ −

SUBAURORAL REGION
(Less Conducting)
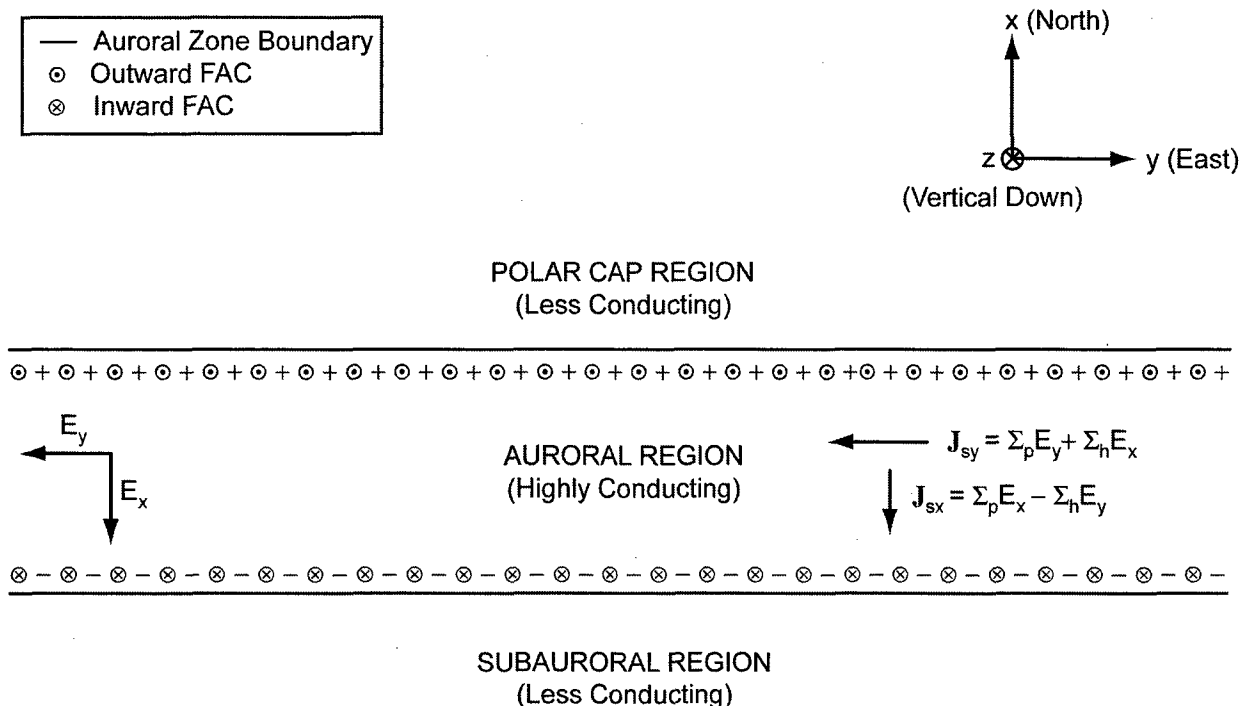
Figure 5-3. Electric Field and Current Structure in the Auroral Region Illustrating the Incomplete Cowling Mechanism

It is well known that FACs flow into and out of the ionosphere in the auroral region and contribute significantly to the coupling between the ionosphere and magnetosphere. Therefore, some of the polarization charges along the boundaries of the auroral zone are carried away in the form of FACs to and from the magnetosphere. Consequently, the southward polarization field in figure 5-3 does not grow sufficiently for the southward Pedersen current to completely cancel the northward Hall current. Thus, the Cowling mechanism for the AEJ is operating ineffectively (reference 21).

To evaluate the effectiveness of the Cowling model to explain the existence of the AEJ, the following ratio is defined (reference 21):

$$\alpha \equiv \frac{\Sigma_p E_x}{\Sigma_h E_y}. \tag{5-5}$$

The parameter α is a measure of the degree of cancellation of the northward Hall current by the southward Pedersen current. The substitution of α into expression (5-4) yields

$$J_{sx} = \Sigma_h E_y (\alpha - 1) \ , \tag{5-6a}$$

and

$$J_{sy} = \Sigma_p E_y \left[1 + \alpha \left(\frac{\Sigma_h}{\Sigma_p} \right)^2 \right] \ . \tag{5-6b}$$

The two extreme cases are (1) the classical Cowling model ($\alpha = 1$), and (2) the "no polarization field" case ($\alpha = 0$). In the classical Cowling model, the substitution of $\alpha = 1$ into formulas (5-6) yields

$$J_{sx} = 0 \ , \tag{5-7a}$$

and

$$J_{sy} = \left(\Sigma_p + \frac{\Sigma_h^2}{\Sigma_p} \right) E_y \equiv \Sigma_c E_y \ , \tag{5-7b}$$

where Σ_c is the height-integrated Cowling conductivity. In the "no polarization field" case, $E_x = 0$. This case can occur only when the FACs remove all of the excess charges carried by the northward Hall current. In actuality, it is anticipated that the FACs take away only some of the excess charges so that the northward Hall current is not entirely cancelled by the southward Pedersen current, i.e., $0 < \alpha < 1$. Kamide (reference 21) refers to this more realistic case as the incomplete or partial Cowling model, and the parameter α is the Cowling efficiency.

Figure 5-4 shows typical altitude profile plots of the electron density n_e and the Pedersen and Hall conductivities for both daytime and nighttime and under quiet and disturbed conditions. Brekke et al. (reference 22) produced these plots via radar-measured electron densities. The plots suggest that the Hall conductivity is sensitive to the electron density at altitudes below 125 km and that the maximum Pedersen conductivity lies in the altitude range from 125–140 km. The maximum Hall conductivity is located in the altitude range from 100–120 km. The plots also show that the Hall conductivity increases significantly under magnetically disturbed conditions. For example, the peak Hall conductivity at nighttime is approximately 5.0×10^{-5} S/m under quiet conditions, as compared with approximately 1.18×10^{-3} S/m under disturbed conditions, an increase by a factor of nearly 24. Also note that the peak Hall conductivity is larger than the peak Pedersen conductivity under each of the conditions described in figure 5-4. The peak electron densities in figure 5-4 occur over a range of altitudes extending from

approximately 95 km (disturbed daytime) to nearly 130 km (quiet nighttime). The daytime plots in figure 5-4 show that the electron densities increase with altitude in the upper part of the E-region.
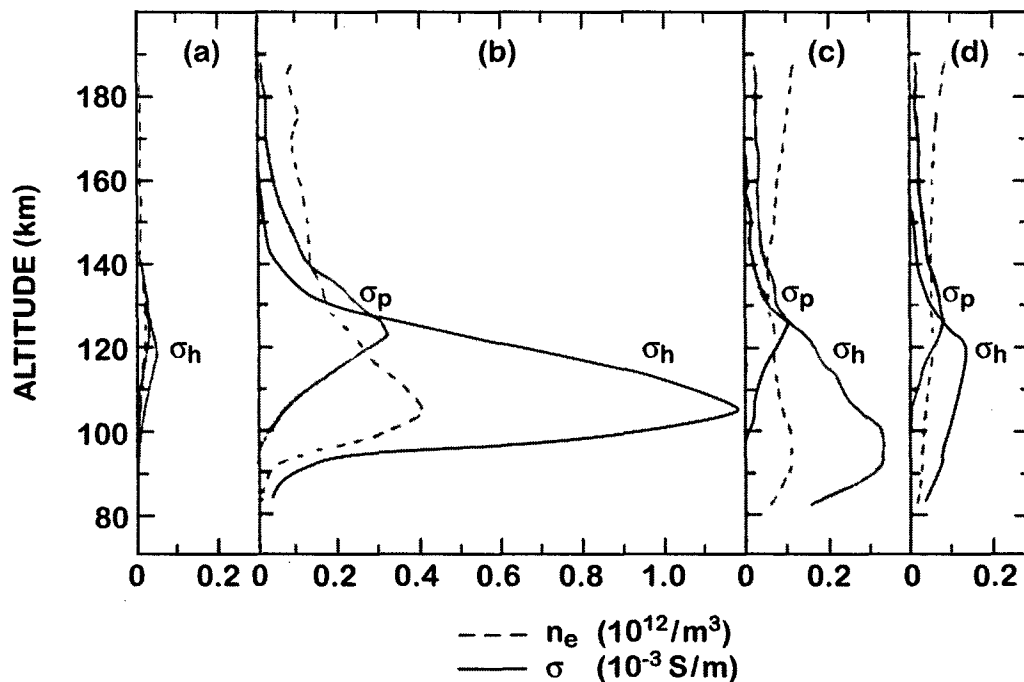

Figure 5-4. Altitude Profiles for Electron Density n_e, Pedersen Conductivity σ_p, and Hall Conductivity σ_h for (a) Quiet Nighttime (8:46 PM LT), (b) Disturbed Nighttime (12:39 AM LT), (c) Disturbed Daytime (1:11 PM LT), and (d) Quiet Daytime (2:10 PM LT) on 13-14 October 1974, as Reported by Brekke et al. (Reference 22)

A comparison of figure 5-4 with figure 3-4 shows that the peak Pedersen and Hall conductivities at the dip equator are approximately 6.3×10^{-4} S/m and 8.5×10^{-4} S/m, respectively, as compared with approximately 7.0×10^{-5} S/m and 1.4×10^{-4} S/m, respectively in the auroral region under quiet daytime conditions. However, under disturbed nighttime conditions in the auroral zone, the peak Pedersen and Hall conductivities are approximately 3.3×10^{-4} S/m and 1.18×10^{-3} S/m, respectively. These comparisons indicate that the peak Pedersen conductivity at the dip equator is about nine times as large as the peak Pedersen conductivity in the auroral region under quiet daytime conditions, but only twice as large as the peak for disturbed nighttime conditions. However, the peak Hall conductivity at the dip equator is approximately six times greater than the peak Hall conductivity in the auroral region under quiet daytime conditions, but is less than the peak Hall conductivity in the auroral region under disturbed nighttime conditions.

The electron density profiles in figures 3-2 and 5-4 yield comparisons that are consistent with those of the peak conductivities. In conclusion, except for disturbed nighttime conditions in the auroral zone, the peak conductivities at the dip equator are greater than the conductivities in the auroral region.

Figure 5-5 presents hourly averages of the electric field components in the auroral zone as a function of local time that were obtained from 32 balloon flights as reported by Mozer and Lucht (reference 23). The plots show that the average peak electric fields in the south and north directions are approximately 33 mV/m and 30 mV/m, respectively, occurring at about 4:00 AM LT and 6:00 PM LT, respectively. The plots indicate that the north-south electric field is larger in magnitude than the east-west electric field for most of the time. Note that the north-south electric field switches direction from southward to northward at about 2:30 PM LT and from northward to southward at approximately 9:30 PM LT.
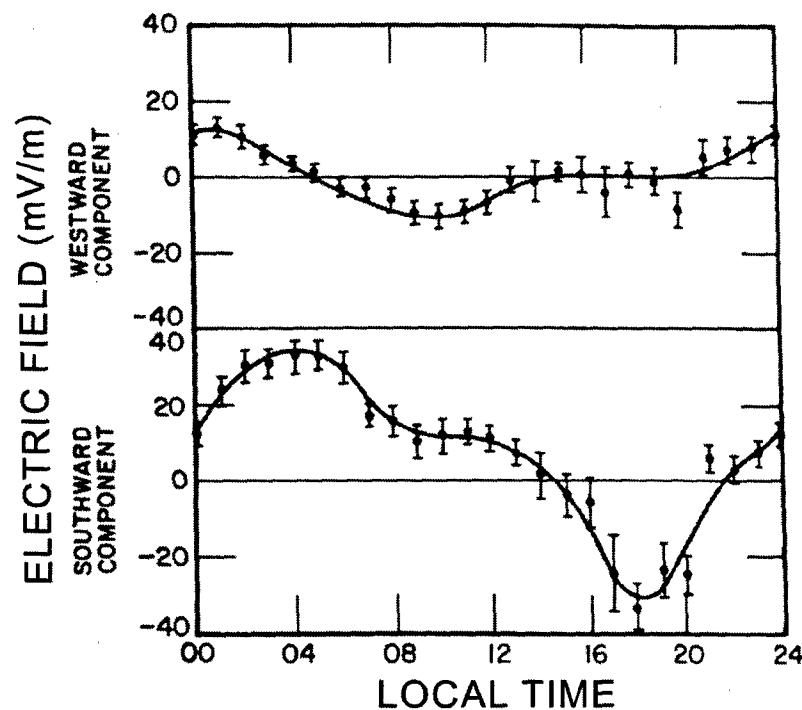

Figure 5-5. Hourly Averages of the Auroral Zone Electric Field Components Measured from 32 Balloon Flights in a Nonrotating Frame of Reference, as Reported by Mozer and Lucht (Reference 23)

54

Figure 5-6 is a plot of the electric field and height-integrated conductivities as a function of time as determined from ionospheric scatter radar measurements at Chatanika, AK, on 16 April 1973 and reported by Kamide and Brekke (reference 24). This day was characterized by the frequent occurrence of polar substorms. Again, the plots show the dominance of the north-south electric field over most of the day, with the southward field appearing in the morning and the northward field in the evening. The north-to-south transition in the electric field occurred in the pre-midnight hours that included several fluctuations. The westward field also fluctuated during the north-to-south field transition and turned eastward after midnight. The height-integrated conductivity plots in figure 5-6 show that the Hall conductivity is much larger than the Pedersen conductivity during the pre-midnight, midnight, and morning periods.
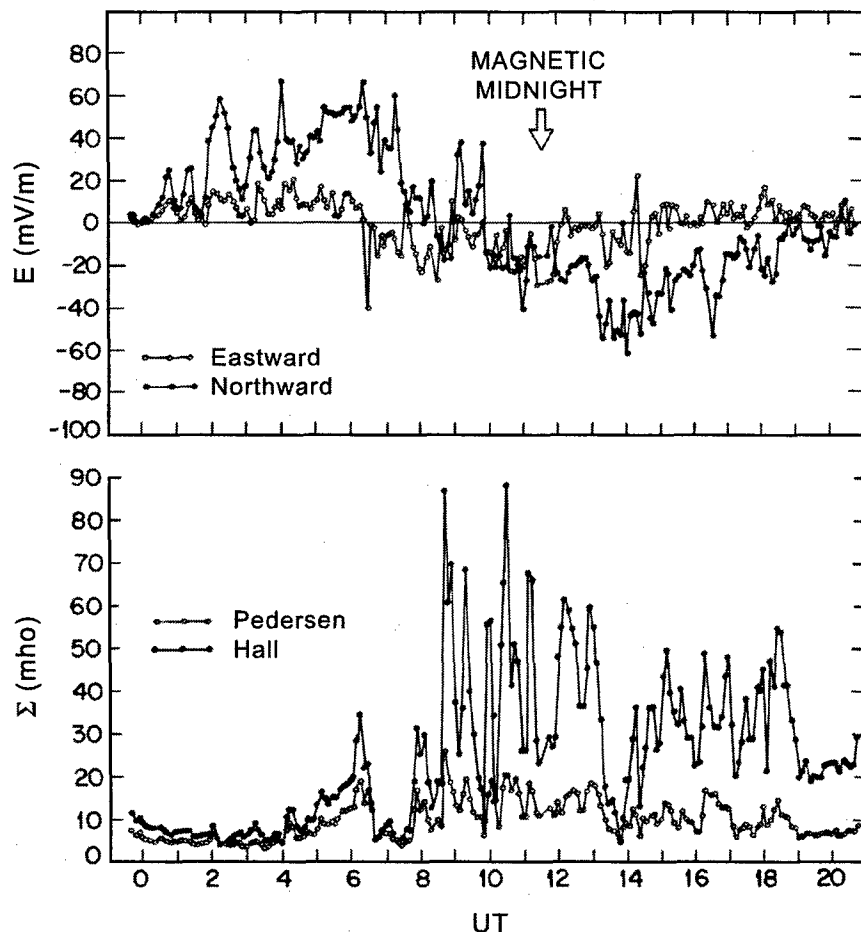

Figure 5-6. Diurnal Variation of the Transverse Ionospheric Electric Field and Height-Integrated Conductivities for 16 April 1973, as Deduced from Chatanika, AK, Ionospheric Radar (64.9° N Latitude) Data by Kamide and Brekke (Reference 24)

The reversal of the electric field from northward to southward is referred to as a Harang discontinuity (reference 21). The Harang discontinuity is attributed to a reversal in the sign of the perturbation in the horizontal geomagnetic field H observed by ground magnetometers. The Harang discontinuity occurs at about 2100–2200 MLT[*] and latitudes vary as a function of time. In the Harang discontinuity region, the electric field gradually changes from northward to southward counterclockwise, where the westward component of electric field normally dominates over the north-south component. In addition, the AEJ changes direction from east to west along the Harang discontinuity.

It can be seen from formula (5-4) and figure 5-6 that the eastward AEJ is controlled primarily by the enhancement of the northward electric field in the evening period. However, the westward AEJ is controlled primarily by the enhancement of the Hall conductivity around midnight. In the late morning period, both the southward electric field and the Hall conductivity determine the intensity of the westward AEJ. A comparison of the north-south electric field in figures 5-5 and 5-6 with the vertical electric field profiles in figures 3-6 and 3-7b shows that the peak north-south electric field in the auroral zone is roughly three to four times greater than the peak vertical electric field at the dip equator. Note that both of these field components are associated with the Hall electrojet currents. According to Kelley (reference 25), the average auroral electric field has an amplitude of 30 mV/m with maxima near 0500 and 1800 LT.

Figure 5-7 shows a contour plot of the horizontal ionospheric current density (A/m^2) as a function of altitude and time, along with a plot of the eastward height-integrated current density (A/m) and corresponding ground-measured H perturbation. In these plots, note that magnetic midnight occurs at approximately 11:00 AM UT. In the contour plot, the dashed line indicates the maximum current density as a function of time. The contours show that the current center of the eastward AEJ is located at higher altitudes (average altitude ~119 km) than that of the westward AEJ (average altitude ~102 km). The maximum current density contour plotted, 40 A/km^2, occurs in the late evening and midnight periods, and corresponds to the spikes in the height-integrated current density plot. These current spikes are attributed to magnetic substorm intensification. During more quiet periods, it appears that the maximum current density may be reduced by as much as a factor of 10. In comparison, table 3-2 indicates that average peak

---

[*]MLT = magnetic local time.

56

current density for the EEJ at the two locations listed is approximately 10 A/km². Therefore, based on this comparison, under magnetically quiet conditions, the current density of the EEJ is comparable or possibly larger than that of the AEJ. However, under magnetically disturbed conditions, the peak AEJ current density can be several times larger than that of the EEJ.
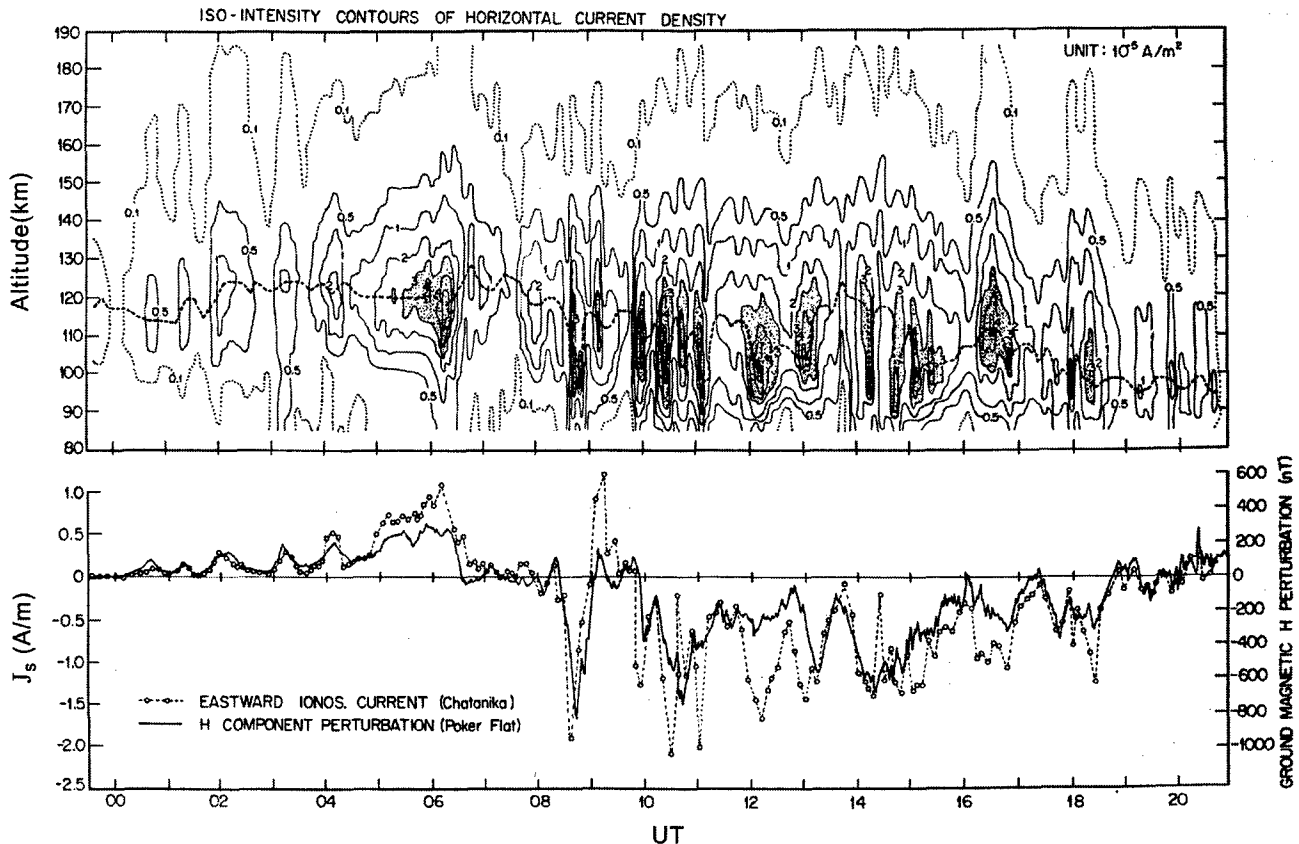
Figure 5-7. Isointensity Contours of (a) Ionospheric Current Density as Function of Altitude and UT over Chatanika, AK (64.9° N Latitude), and (b) Height-Integrated Ionospheric Current Density over Chatanika, AK, and the Corresponding H Component Perturbation at Poker Flat, AK (64.9° N Latitude) (Measurements Taken on 16 April 1973 and Reported by Kamide and Brekke, Reference 24)

The bottom plot in figure 5-7 indicates the presence of an eastward current during the afternoon and evening hours and a westward current from approximately 2 hours before midnight through most of the morning period. The roughly 2-A/m spikes in the height-integrated westward current are approximately twice as large as the eastward current spikes. In comparison, table 3-2 indicates that average peak height-integrated current density for the EEJ at the two locations listed is approximately 0.14 A/m, approximately an order of magnitude less than the AEJ spikes under magnetically disturbed conditions. However, under magnetically

quiet conditions, it is anticipated that the height-integrated current densities EEJ and AEJ will be more comparable in magnitude.

Kelley (reference 25) indicated that the AEJ is characterized by a localized height range of current rather than a narrow latitudinal range that is characteristic of the EEJ. The AEJ has a finite width that is typically about 5° or 6° in latitude (reference 26). According to Kamide (reference 21), two common models have been used to describe the current distribution of the AEJ, namely, a line current model and a sheet current model. The line current model was originally used in estimating the height of the AEJ, but yielded altitudes that were too high. The sheet current model of the AEJ with finite latitudinal width has been useful in estimating the magnitude and width of the AEJ. Boteler et al. (reference 26) showed that a sheet current model with a Cauchy distribution current density is a suitable representation of the AEJ.

A better perspective of the electric field and horizontal height-integrated ionospheric current distribution in the auroral region can be obtained from the results of an analytical model developed by Zhang and Carovillano (reference 27). In this model, the ionosphere is assumed to be a thin, spherical conducting shell that is electrically neutral and highly conducting. In addition, because the analysis is confined to high latitudes, the geomagnetic field is assumed to be pointed radially inward and have constant magnitude in the northern hemisphere. Because the observed pattern of the FAC appears to have a narrow latitude extension in statistical representations, Zhang and Carovillano represented the FAC by two sets of sheet currents located at constant colatitudes $\theta_1 = 18°$ (polar cap boundary) and $\theta_2 = 26°$ (equatorial boundary of the auroral region). The Hall-to-Pedersen height-integrated conductivity ratio (Σ_h/Σ_p) is denoted by Σ, and the ratios of the Pedersen conductivities in the different zones are defined by

$$p_1 \equiv \frac{\Sigma_p^I}{\Sigma_p^{II}}, \quad p_3 \equiv \frac{\Sigma_p^{III}}{\Sigma_p^{II}}, \tag{5-8}$$

where Σ_p^I, Σ_p^{II}, and Σ_p^{III}, refer to the height-integrated Pedersen conductivities in the polar cap, auroral zone, and sub-auroral zones, respectively. An enhanced auroral conductivity is represented by $p_1 < 1$ and $p_3 < 1$. The model enforces the current continuity equation throughout the ionosphere and requires that the electric scalar potential V satisfies the boundary condition

$$V(\theta = \theta_1) = V_1 \sin \varphi, \tag{5-9}$$

where V_1 is half of the polar cap driving potential and φ is the azimuthal angle measured counter-clockwise from the magnetic meridian. Note that the potential distribution (5-9) accounts for the dawn-to-dusk electric field inside the polar cap. The potential V_2 is the maximum value of the electric potential at $\theta = \theta_2$.

Figure 5-8 shows vector plots of the electric field and the horizontal height-integrated ionospheric current in the polar cap and auroral zones that were determined from the analytical model of Zhang and Carovillano (reference 27). (See figure 5-8 for the input parameters.) The pairs (I_1, δ_1) and (I_2, δ_2) refer to the amplitude and phase of the total return FAC located at the zonal boundaries $\theta = \theta_1$ and $\theta = \theta_2$, respectively. Figure 5-8(a) shows that inside the polar cap ($\theta < 18°$) the electric field is directed from dawn to dusk, is independent of azimuth, and has a constant magnitude of 15 mV/m. In the sub-auroral region ($26° < \theta < 40°$), the electric field is directly proportional to V_2, is independent of azimuth, decreases from high to low latitudes, and is significantly less than in the auroral zone ($18° < \theta < 26°$). In the auroral zone, the electric field varies significantly in both latitude and azimuth and is very large, with an average magnitude about twice that in the polar cap. In the auroral zone, the electric field is a maximum around dawn (6:00 AM LT) and dusk (6:00 PM LT) and decreases with azimuth with its weakest intensity around local noon and midnight.

In figure 5-8(b), the AEJ current flows westward in the morning and eastward in the afternoon and evening. According to Zhang and Carovillano (reference 27), the AEJ current is very intense because of the combined effects of the conductivity enhancement in the auroral zone and the return current at the equatorial boundary of the auroral region. The height-integrated ionospheric current in zones I, II, and III varies with azimuth, in a manner similar to the electric field. It should be mentioned that the Pedersen current flows along the direction of the electric field and connects the FAC located along the boundaries of the auroral zone at $\theta = \theta_1$ and $\theta = \theta_2$. As previously mentioned, it is the stronger Hall current in the auroral region that is primarily responsible for the eastward and westward AEJs. Zhang and Carovillano's model has a 180° rotational balance; i.e., the total AEJ current flowing eastward at one LT near the dusk sector equals the total AEJ current flowing westward 12 hours later in the dawn sector.
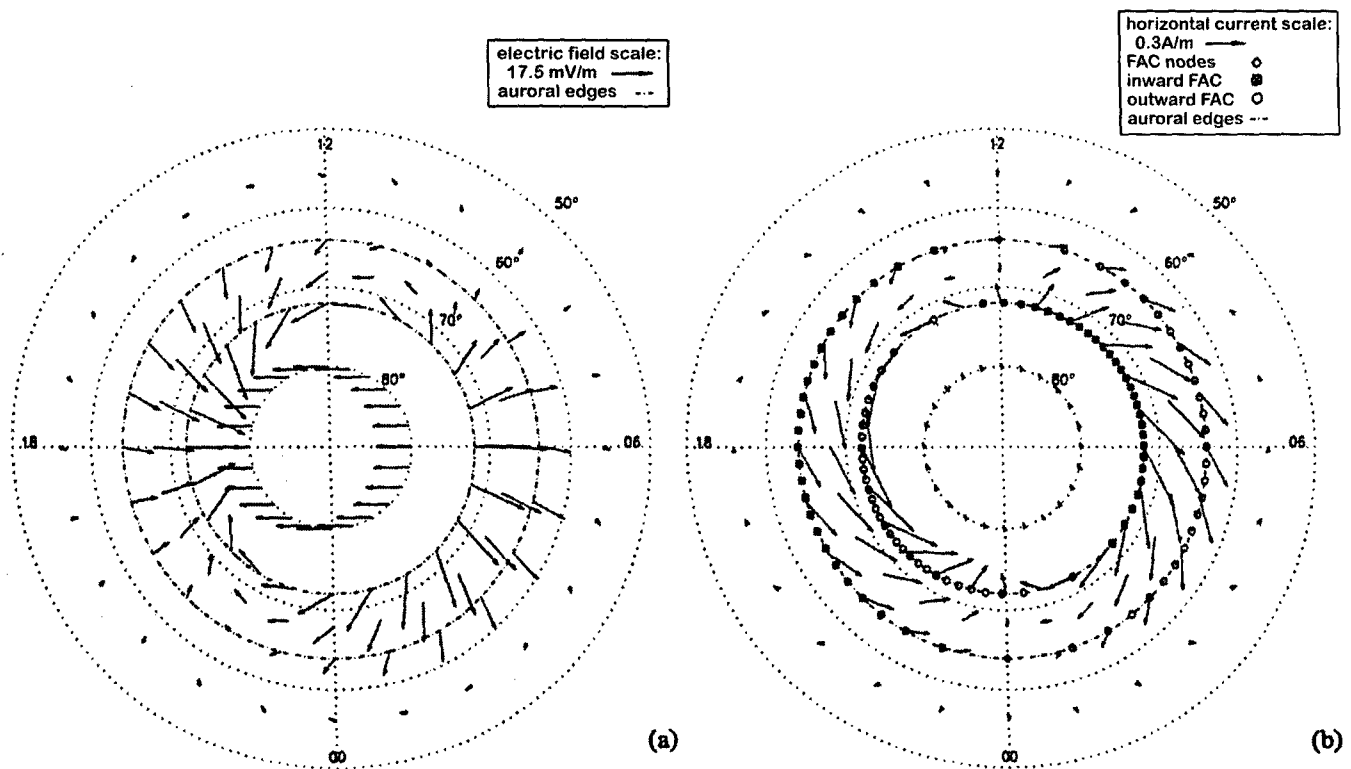
Plots are based on the following parameters: V_1 = 30 kV, p_1 = p_3 = 0.2, Σ = 2.0;

(a) I_2 = 0.5 MA, δ_2 = $-10°$, Σ_p = 10; (b) I_1 = 1.18 MA, I_2 = 1.0 MA, δ_1 = 28°, δ_2 = 0°, Σ_p = 5.

***Figure 5-8. Vector Plots of the (a) Electric Field and
(b) Height-Integrated Ionospheric Current***
(Taken from Zhang and Carovillano (reference 27), p. 95)

Figure 5-9 is a rough sketch presented by Kamide (reference 21) that shows the relative
contributions of the electric field and ionospheric conductivity to the eastward- and westward-
directed AEJ. The eastward EEJ is centered at approximately 66.0°–66.5° N latitude and is
dominated by the northern component of electric field. Near local midnight and the early
morning hours, the AEJ is directed westward and is characterized by a large Hall conductivity,
attributed to magnetic substorms. In contrast, in the late morning hours, the westward AEJ is
dominated by a large southern component of electric field. The drawing shows the Harang
discontinuity as the region where the AEJ switches from eastward to westward. In the region
just eastward of the Harang discontinuity, the poleward portion of the AEJ is westward with an
electric field composed of south and west components in contrast to the equatorward portion of
the AEJ that is eastward-directed, with a large north component of electric field. Figure 5-9
indicates that in the early morning period (1:00 AM - 3:00 AM MLT) the poleward portion of

the westward AEJ is dominated by strong southward electric field while the equatorward portion is dominated by a large Hall conductivity. In the midnight period, the westward AEJ is centered at approximately 66.5°–67.0° N latitude; in the late morning period, the westward AEJ is centered at approximately 65.2° N latitude.
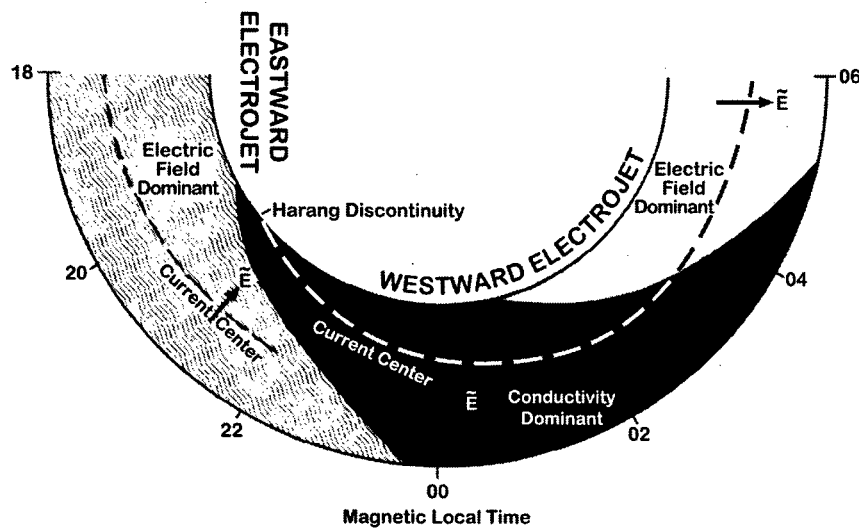

Figure 5-9. Schematic Diagram Showing the Relative Importance of the Ionospheric Conductivity and the Electric Field in the Eastward and Westward Electrojets
(Taken from Kamide (reference 21), p. 669)

6. GENERATION OF LOW-FREQUENCY SIGNALS FROM A HEATED AND MODULATED EEJ

In the attempt to transmit low-frequency electromagnetic radiation into the earth-ionosphere waveguide from a heated and modulated ionosphere, the EEJ possesses some unique features. According to Papadopoulos et al. (reference 28), some of the advantages of generating ELF and VLF signals from a heated EEJ over a heated AEJ are listed below.

1. The equatorial electron density profiles are better suited to heating at high altitudes, resulting in higher heating efficiency and reduced absorption.

2. Equatorial heating creates a significant vertical electric dipole (VED) that couples much more efficiently (factors of 103-104) to the earth-ionosphere waveguide than the horizontal magnetic dipole (HMD) produced via auroral heating.

3. The ducted VLF produced by equatorial heating allows for whispering gallery type propagation with very low attenuation in the 1-4 kHz range rather than loss into the magnetosphere. The ducted VLF can propagate along the E-region with lower attenuation than in the earth-ionosphere waveguide, resulting in large coverage along the magnetic meridian.

In summary, according to Papadopoulos et al. (reference 28), at the equator the same heating power should generate significantly more radiated ELF/VLF signal power with better reliability than is currently produced at the existing polar facilities.

The first reported experiments found in the literature involving the radiation from a heated and modulated EEJ current system is given in a paper by Lunnen et al. (reference 29). These experiments involved the Jicamarca VHF radar facility located approximately 11 km east of Lima, Peru, and the Arecibo, Puerto Rico, HF transmitter located 5 km east of Islote, Puerto Rico. Two heating experiments involving the EEJ were performed, i.e., a long-range experiment in September 1982 and a short-range experiment in May 1983. Both heating experiments were performed at midday when there is a strong electrojet current.

The long-range experiment involved heating the EEJ with the Jicamarca radar with a linearly polarized wave of effective radiated power (ERP) equal to 5,547 MW, carrier frequency of 49.92 MHz, 2° beamwidth, and modulated at a 5% duty cycle with a square wave of frequency 2.5 kHz

(VF band) (reference 30). The radar was operated on a heating/cooling cycle of 2 minutes on/2 minutes off. It was reported that the radiated signal was received at Salinas, Puerto Rico, located approximately 67 km southeast of the Islote transmitter and 3.532 Mm from the Jicamarca facility. The received signal at Salinas showed a dominant amplitude at 4.17 mHz in the 2.5-kHz FFT that corresponded to the on/off period of 240 seconds. However, as expected, the signal amplitude was much smaller than the local signal produced by the Arecibo transmitter operating with an ERP of 160–320 MW, a 3.170-MHz carrier frequency, and modulated at a 50% duty cycle. At a recent workshop on ionospheric measurements (reference 31), several experts questioned the validity of these measurements.

The short-range experiment involved heating and modulating the EEJ with the Jicamarca radar near local noon under the same conditions as in the long-range experiment. The receiver was located approximately 9 km south of the Jicamarca facility. The received signal was an order of magnitude less than a typical local signal produced by the Arecibo heating facility. This difference in signal levels is attributed by Lunnen et al. (reference 29) to the narrower beamwidth, higher heating frequency, and lower duty cycle of the Jicamarca radar as compared with the Arecibo transmitter, where the parameters are more optimum. The short-range experiment helped to characterize the signal radiated from a heated and modulated ionospheric current system near the mid-latitudes.

At the time of publication of this report, Papadopoulos et al. (reference 32) presented results from some recent EEJ heating experiments performed with the Jicamarca 49.92 MHz incoherent scatter radar transmitter facility. They reported that the measurement site in Pueblo, Peru, used by Lunnen et al. (reference 29) in their 1983 short-range experiment was contaminated by signals generated by the modulated currents in the wires of the VHF transmitter and as a result, no reliable measurements could be taken there. From their recent EEJ heating experiments in September and October 2004, Papadopoulos et al. (reference 32) reported the detection of VLF signals at Ancon, Peru, of approximately 3 fT (femto-tesla) at 3.2 and 4.0 kHz. The measured time delay of the direct-path signal and its amplitude were observed to be consistent with their theoretical model. In addition, Papadopoulos et al. (reference 32) reported the first detection of whistler-mode signals of approximately 2.4 fT at 3.2 and 4.0 kHz with a delay time consistent

with their model. From these experiments, Papadopoulos et al. (reference 32) concluded that their models would also accurately predict the signals that will be received if they were to use an HF heater. Based on the results of simulations, Papadopoulos et al. (reference 32) indicated that 100 kW is the minimum useful HF heating power for the transmission of VLF signals in the equatorial region.

The above experiments suggest that it may be feasible to generate ELF/VLF signals from a heated and modulated EEJ. However, an organized effort will be required that involves more optimum heating and signal parameters.

7. CONCLUSIONS

This report has presented an overview of the characteristics of the equatorial electrojet (EEJ), auroral electrojet (AEJ), and the worldwide dynamo current system. The results have shown that the EEJ is a direct current of high intensity that flows along the eastward direction at a mean altitude of 106 km over a narrow region surrounding the dip equator. The EEJ is generally most intense over a 4-hour time span that is centered about local noon and does not normally exist at nighttime. The primary component of the EEJ current is associated with the geomagnetic solar quiet daily variation Sq. Sq currents in the ionosphere are a major contributor to the diurnal variation observed in the geomagnetic field. In the region surrounding the dip equator, two current layers have been observed: the lower layer is the EEJ and the upper layer is associated with the worldwide part of the Sq current system or WSq. Results have suggested that the EEJ is more stable than the other ionospheric current systems.

Both the EEJ and AEJ are Hall-driven currents that exist in the E-region of the ionosphere. However, the AEJ seems to be more complicated because it is affected by the frequent magnetic substorms that occur in the auroral oval region. These substorms affect both the electric field and conductivities in the E-region. During magnetically disturbed periods, the results in this report indicate that the peak westward AEJ current density near local midnight can be several times larger than the maximum EEJ current. However, during magnetically quiet periods, the EEJ may have a greater peak intensity than that of the AEJ.

Several experiments have been reported regarding the generation of low-frequency signals from a heated and modulated EEJ. Although the validity of the first reported measurements by Lunnen et al. (reference 29) have been questioned by some experts (reference 31), the results of recent experiments reported by Papadopoulos et al. (reference 32) suggest that it may be possible to transmit ELF or VLF signals by this means. However, the selection of more optimum heating and signal parameters will be required to make this implementation feasible.

8. REFERENCES

1. J. Egedal, "The Magnetic Diurnal Variation of the Horizontal Force Near the Magnetic Equator," *Terrestrial Magnetism and Atmospheric Electricity*, vol. 52, 1947, pp. 449-451.

2. J. Egedal, "Daily Variation of the Horizontal Magnetic Force at the Magnetic Equator," *Nature*, vol. 161, 1948, pp. 443-444.

3. S. Chapman, "Some Phenomena of the Upper Atmosphere," *Proceedings of the Physical Society of London B*, vol. 64, 1951, pp. 833-843.

4. C. A. Onwumechili, *The Equatorial Electrojet*, Gordon and Breach Science Publishers, Amsterdam, The Netherlands, 1997.

5. D. F. Knecht, "The Geomagnetic Field, A Revision of Chapter 11 of *Handbook of Geophysics and Space Environments*," S. L. Valley, ed., AFCRL-72-0570, Air Force Surveys in Geophysics, No. 246, Air Force Cambridge Research Laboratories, L. G. Hanscom Field, Bedford, MA, 26 September 1972.

6. H. Rishbeth and O. K. Garriott, *Introduction to Ionospheric Physics*, Academic Press, New York, 1969.

7. S. Matsushita and H. Maeda, "On the Geomagnetic Solar Quiet Daily Variation Field During the I.G.Y.," *Journal of Geophysical Research*, vol. 70, 1965, pp. 2535-2558.

8. A. Ishimaru, *Electromagnetic Wave Propagation, Radiation, and Scattering*, Prentice Hall, Englewood Cliffs, NJ, 1991, Ch. 8.

9. B. H. Subbaraya, P. Muralikrishna, T. S. G. Sastry, and S. Prakash, "A Study of the Structure of Electrical Conductivities and the Electrostatic Field within the Equatorial Electrojet," *Planetary Space Science*, vol. 20, 1972, pp. 47-52.

10. J. M. Forbes and R. S. Lindzen, "Atmospheric Solar Tides and Their Electrodynamic Effect—I. The Global Sq Current System," *Journal of Atmospheric and Terrestrial Physics*, vol. 38, 1976, pp. 897-910.

11. S. Matsushita, "Dynamo Currents, Winds, and Electric Fields," *Radio Science*, vol. 4, 1969, pp. 771-780.

12. R. Dendy (ed.), *Plasma Physics: An Introductory Course*, Cambridge University Press, Cambridge, U.K., 1993, Ch. 1.

13. J. Sartiel, "Champs Electrques Dan La Region de L'electrojet Equatorial," Ph.D. Thesis, University of Paris VI, France, 1977.

14. D. Ivers, R. Stening, J. Turner, and D. Winch, "Equatorial Electrojet from Ørsted Scalar Magnetic Field Observations," *Journal of Geophysical Research*, vol. 108, no. A2 1061, doi:10.1029/2002JA009310, 2003.

15. H. Luhr, S. Maus, and M. Rother, "Noon-Time Equatorial Electrojet: Its Spatial Features as Determined by the CHAMP Satellite," *Journal of Geophysical Research*, vol. 109, no. A01306, doi:10.1029/2002JA009656, 2004.

16. R. F. Pfaff, M. H. Acuna, and P. A. Marionni, "DC Polarization, Electric Field, Current Density, and Plasma Density Measurements in the Daytime Equatorial Electrojet," *Geophysical Research Letters*, vol. 24, no. 13, July 1, 1997, pp. 1667-1670.

17. S. E. Forbush and M. Casaverde, *The Equatorial Electrojet in Peru*, Publication 620, Carnegie Institute of Washington, Washington, DC, 1961.

18. N. C. Maynard, "Measurement of Ionospheric Currents off the Coast of Peru," *Journal of Geophysical Research*, vol. 72, 1967, pp. 1863-1875.

19. G. Jadhav, M. Rajaram, and R. Rajaram, "A Detailed Study of Equatorial Electrojet Phenomenon using Ørsted Satellite Observations," *Journal of Geophysical Research*, vol. 107, no. A8, 1175, doi:10.1029/2001JA000183, 2002.

20. B. M. Shuman, "Rocket Measurement of the Equatorial Electrojet," *Journal of Geophysical Research*, vol. 75, 1970, pp. 3889-3901.

21. Y. Kamide, *Electrodynamic Processes in the Earth's Ionosphere and Magnetosphere*, Kyoto Sangyo University Press, Kyoto, Japan, 1988.

22. A. Brekke, J. R. Doupnik, and P. M. Banks, "Incoherent Scatter Measurements of E Region Conductivities and Current in the Auroral Zone," *Journal of Geophysical Research*, vol. 79, 1974, pp. 3773-3790.

23. F. S. Mozer and P. Lucht, "The Average Auroral Zone Electric Field," *Journal of Geophysical Research*, vol. 79, no. 7, 1974, pp. 1001-1006.

24. Y. R. Kamide and A. Brekke, "Altitude of the Eastward and Westward Auroral Electrojets," *Journal of Geophysical Research*, vol. 82, no. 19, 1977, pp. 2851-2853.

25. M. C. Kelley, *The Earth's Ionosphere: Plasma Physics and Electrodynamics*, Academic Press, San Diego, CA, 1989.

26. D. H. Boteler, R Pirjola, and L. Trichtchenko, "On Calculating the Electric and Magnetic Fields Produced in Technological Systems at the Earth's Surface by a Wide Electrojet," *Journal of Atmospheric and Solar-Terrestrial Physics*, vol. 62, 2000, pp. 1311-1315.

27. L. Zhang and R. L. Carovillano, "Plasma Convection and Currents in the Auroral Zone," in *Auroral Plasma Dynamics* (R. L. Lysak, ed.), Geophysical Monograph 80, American Geophysical Union, Washington, DC, 1993, pp. 89-96.

28. D. Papadopoulos, T. Wallace, G. Milikh, and B. Peter, "Equatorial ELF/VLF Generation," presented at the HAARP ELF Measurements Workshop, High Frequency Active Auroral Research Program, Arlington, VA, 4-5 November 2004.

29. R. J. Lunnen, H. S. Lee, A. J. Ferraro, T. W. Collins, and R. F. Woodman, "Detection of Radiation from a Heated and Modulated Equatorial Electrojet Current System," *Nature*, vol. 311, no. 13, September 1984, pp. 134-135.

30. E. C. Jordan, ed., *Reference Data for Radio Engineers: Radio, Electronics, Computer, and Communications*, Seventh Edition, Howard W. Sams & Co., Indianapolis, IN, 1985, p. 1-3 (chap. 1).

31. HAARP ELF Measurements Workshop, High Frequency Active Auroral Research Program, Arlington, VA, November 4-5, 2004 (see http://www.haarp.alaska.edu).

32. D. Papadopoulos, T. Wallace, B. Peter, G. Milikh, D. Manion, and J. Berry, "ELF Generation and Propagation: Polar vs. Equatorial," presented at the Eleventh Annual RF Ionospheric Interactions Workshop, Santa Fe, NM, 17-20 April 2005.

INITIAL DISTRIBUTION LIST

Addressee	No. of Copies
Office of Naval Research (ONR-312, E. Kennedy)	1
Naval Research Laboratory (P. Bernhardt, P. Rodriguez)	2
Air Force Research Laboratory (P. Kossey, K. Groves)	2
Science Applications International Corporation (P. Bannister, R. Ingram, D. Miller)	3
University of Alaska at Fairbanks (D. Solie, A. Otto, D. Sentman)	3
Stanford University (T. Bell, U. Inan, A. Fraser-Smith, R. Moore)	4
Pennsylvania State University (J. Breakall, A. Ferraro, D. Werner)	3
University of Maryland (G. Milikh, D. Papadopoulos)	2
University of Connecticut (R. Bansal)	1
Geospace Research Inc. (F. Djuth)	1
BAE Systems (M. McCarrick, T. Wallace)	2
Defense Technical Information Center	2
Center for Naval Analyses	1